Master of Science Thesis
VT2019

Optimization of Acquisition Time for 177-Lu SPECT with Two Energy Windows

Fanny Mörnsjö Centofanti

Supervisors

Johan Gustafsson, Katarina Sjögreen Gleisner, Daniel Roth och Michael Ljungberg

Department of Medical Radiation Physics,
Faculty of Science
Lund University
www.msf.lu.se

Abstract

Background & Aim: The imaging process following the treatment of ^{177}Lu-DOTATATE is in some medical clinics demanding on both patients and the clinic. Usually a number of images are acquired, with different time intervals to the time of injection. To facilitate for the patient and create the opportunity to treat more patients it is desirable to simplify the imaging process. At Skåne University hospital (SUS) the number of imaging sessions has been reduced from four to one, acquired 96 hours p.i. Image acquisition is done with SPECT imaging, which is used for determination of absorbed dose. The main objective is a SPECT image of the kidneys, but there is also a great interest to map out the absorbed dose to tumours. In order to do so a two FOV SPECT image has to be acquired. Thus the total acquisition time becomes very long and patient movements has shown to be a great difficulty when matching the two FOV together.

At SUS image acquisition is made with one energy window around the 208 keV photopeak and by adding a second one around the 113 keV photopeak, the acquisition time can hopefully be reduced. The determination of absorbed dose is based on a mean value of the activity concentration inside a VOI defined from CT image. Thus the task is to lower the acquisition time but still maintain a mean value with low uncertainty. This results in the question formulation: For SPECT imaging, of patients treated with ^{177}Lu-DOTATATE, how much can the acquisition time be reduced when collecting information from 113 keV photopeak and 208 keV photopeak?

Method: SPECT projection data of a cylindrical phantom, within it 6 spheres of different sizes, were simulated with Monte Carlo code SIMIND. Projection sets with activity in the spheres and activity in the background were simulated separately and added together in a later step. The reason for the separate simulation was to easily be able to modify the activity concentration in the spheres and background independent of each other. Different number of counts in the projection data can be a result of either different activity concentrations in source regions or due to different acquisition times. A quantity, named ”disintegration concentration value”, was defined as the number of radioactive decay during the acquisition time, per unit volume, to be able to change the acquisition time in the projection data. The disintegration concentration in the spheres was changed by multiplying with so called Disintegration Concentration value (DC-value) [MBq·s/ml], derived from activity concentration multiplied with an acquisition time. Thus a higher DC-value is derived from a longer acquisition time, therefore the spheres obtained a higher disintegration concentration. A set of 10 projection sets were created, all multiplied with different DC-values, i.e. different time per projection. The projection data of the sphere and background were added together and four different contrasts of disintegration concentration, between the spheres and the background, were evaluated for all 10 DC-values. For every projection set 50 noise realisation were created. Reconstruction was done with OS-EM algorithm, using 6 subsets and 40 iterations. Projection data for 113 keV and 208 keV were simulated separately and data from the reconstructed images were later added together. Masks of the spheres was created to extract data from the reconstructed images. The data were evaluated by the recovery of the activity concentration and CV, where the standard deviation, of the 50 mean values from the 50 noise realisations, was divided with both the measured disintegration concentration and the true disintegration concentration, respectively.

Result & Conclusion: Image acquisition with two energy windows, one around the 113 keV photopeak and one around 208 keV photopeak, results in time per projections according to DC-value=22.50 MBq·s/ml. For tumours it indicates a time per projection of 22.5 seconds but for kidneys the time per projection would have to be 225 seconds, due to its lower activity concentration 96 hours p.i. compared to the activity concentration in tumours at that time. At SUS the time per projection is 45 seconds, meaning that for image acquisition of tumours the time per projection can be shortened by a factor 2. However for image acquisition of kidneys the time per projection needs to be prolonged by a factor 5 compared to today’s image protocol.

Hur snabbt får man tillräckligt med bildinformation?

Ur ett samarbete mellan biokemi och strålningsfysik har den nuklearmedicinska grenen växt fram. Genom kemiska reaktioner kan man binda radioaktiva atomkärnor till ämnen som i människokroppen har en målsökande egenskap gentemot specifika delar i kroppen. På så sätt riktas ett läkemedel mot ett önskat område, exempelvis ett organ eller receptorer som som uttrycks på bland annant tumörceller.

När den radioaktiva atomkärnan sönderfaller och strålning emitteras skadas tumörvävnaden och tumören kan hämmas. Ur ett diagnostiskt syfte önskar man få en visuell bild över hur läkemedlet har fördelat sig i kroppen. Detta åstadkommer man med hjälp av en Single Photon Emission Computed Tomographic system, så kallad SPECT. Systemet använder sig av den energi, i form av fotoner, som frisläpps vid sönderfallet av den radioaktiva atomkärnan för att skapa bilden. För att erhålla en tillräckligt bra bild för det avsedda ändamålet måste SPECT-systemet utsättas för en tillräcklig mängd fotoner. Det innebär att bildtagningen tar en viss tid, i de flesta fall omkring 30 minuter. Dagens bildtagning är mycket krävande för patienterna, då de måste ligga helt stilla under hela bildtagningen och i samband med att antalet patienter ökar sätter bildtagningstiden en gräns för hur många patienter sjukhuset kan ta emot.

I detta arbete är det en typ utav nuklearmedicinsk behandling som är i centrum, nämligen behandling med ^{177}Lu-DOTATATE. Den radioaktiva atomkärnan förkortas ^{177}Lu, som binds till den receptorsökande peptiden, TATE, med hjälp av ett kelat kallat DOTA. Läkemedlet används för behandling av neuroendokrina tumörer, vilket är ett samlingsnamn för tumörer som härstammar från neuroendrokrina celler. På dessa tumörer sitter somostatinreceptorer som peptiden TATE binder till. När ^{177}Lu sönderfaller kommer strålningen, kallat betastrålning, ge upphov till den terapeutiska effekten med behandlingen och strålningen i form att fotoner användas som informationsbärare för SPECT-systemet att skapa en bild. Genom bilden kan man se hur läkemedlet har fördelat sig i kroppen och man vill kunna mäta ståldosen som njurar och tumörer erhåller. Framförallt är stråldosen till njurarna av intresse, då det sätter gränsen för hur många gånger behandlingen kan ges till en patient.

Då ^{177}Lu sönderfaller kan fotonerna erhålla olika energier. Vilka energierna fotonerna får beskrivs av en statistisk fördelning, där vissa fotonenergier är vanligare än andra. Vid dagens bildtagning, på Skånes Universitetssjukhus (SUS), samlar man endast in information från en av ^{177}Lu möjliga fotoner, nämligen den mest förekommande fotonen med energin 208 keV. Dock finns det även en annan relativt vanligt förkommande foton vid ^{177}Lu-sönderfall, en foton med energin 113 keV. Genom att samla in information från båda dessa fotoner är förhoppningen att en fullgod bild kommer uppnås under en kortare bildtagningstid.

I den insamlade signalen finns, tillsammans med information till bilden, statiska fluktuationer, även kallat brus, tillsammans med den önskade signalen. Vid längre insamlingstider kommer den önskade signalen vara högre i förhållande till bruset, men i samband med att insamlingstiden förkortas kommer skillnaden mellan önskad signal och brus minska. Det innebär att vid för korta insamlingstider kommer den önskade signalen inte synas i bilden, då den drunknar i bruset.

Genom att immitera bildtagningsprocessen med en dator kan man undersöka hur ändringar av olika parametrar påverkar bruset och slutresultatet av bilden. I arbetet ändras parametern bildtagningstid, för att avgöra hur mycket den kan förkortas då man samlar in information från båda fotonrena för att skapa bilden. Målet är att på så kort bildtagning som möjligt erhålla en bild där stråldosen till njurar och tumörer kan mätas med stor säkerhet.

Resultaten i detta arbete visar att ur perspektivet av bildtagning av tumörer, kan bildtagningstiden halveras jämt emot dagens bildtagningstid. Då det framförallt är njurarna man är intresserad av är det den bildtagningstid som njurarna kräver, för en säker uppskattning av stråldosen, som sätter gränsen för hur kort bildtagningen kan bli. Vid bildtagningen är koncentrationen av läkemedel generellt är lägre i njurarna i förhållande till tumörerna, vilket innebär att längre bildtagning krävs för att kunna uppskatta stråldosen till njurarna. Ur perspektivet av njurarna visar resultatet att dagens bildtagningstid behöver förlängas med en faktor 5 för att kunna mäta stråldosen med stor säkerhet.

Contents

Abbreviation

- VOI - Volume of interest
- CT - Computed Tomography
- SUS - Skåne University hospital
- p.i - post injection
- SPECT - Single Photon Emission Computed Tomography
- FOV - Field of view
- ^{177}Lu - ^{177}Lutetium
- PET - Positron Emission Tomography
- OS-EM - Ordered Subset Expectation Maximization
- ML-EM - Maximum Likelihood Expectation Maximization
- LOF - Likelihood objective function
- SD - Standard deviation
- SNR - Signal to Noise ratio
- PVE - Partial Volume effect
- PVC- Partial Volume correction
- ESSE - Effective Scatter Source Estimation
- MC - Monte Carlo
- CRFC - Collimator Response Function Compensation
- DC-value - Disintegration Concentration value
- CV - Coefficient of Variation

1 Introduction

1.1 Background & Aim

For many years the nuclear medicine research group at the Lund University Department of Medical Radiation Physics has been developing a method to, with high accuracy, determine the absorbed dose of organs and tumours. The method uses the mean value of the activity concentration inside a predefined volume of interest (VOI), manually defined with guidance from Computed Tomography (CT) images. In corporation with Skånes University Hospital (SUS) the research group has preformed a clinical trial of treatment of neuroendocrine tumours with ^{177}Lu-DOTATATE, where the administered activity is regulated after the absorbed dose in the patients kidneys. As the treatment is moving from clinical trial to clinical practice, the dosimetry protocol needs to be simplified to one image session instead of four. Based on the conclusion from a study done by Hänscheid et al. the approximation of absorbed dose is best estimated from image taken 96 h post injection (p.i) [9]. Determine the absorbed dose of the kidneys are the main objective, but the absorbed dose of tumours are also of great interest. The desire to map out the uptake in tumours leads to an image acquisition with two field of views (FOV), in order to get a Single Photon Emission Computed Tomography (SPECT) image from the neck down to the most part of the thighs. Matching the two FOV to one image has shown to be a hard task, mainly due to patient movements. Today's image protocol results, with two FOV, in a total acquisition time of 45 minutes. The image acquisition is done with an energy window width of 15 % around 208 keV, using only the most commonly occurring gamma photon from ^{177}Lu.

The aim of this study is to determine if the acquisition time can be shortened, and to what extent, by adding a second energy window around the 113 keV photopeak. At this time few studies have focused on the effects of noise on the uncertainty in the activity quantification in SPECT images. But there is one similar study by He and Frey [6], looking at the effects of precision of quantitative estimates of organ activity as the acquisition is shortened, for SPECT with ^{111}In. Testing scans of 30 minutes acquisition time down to 1,5 minutes they found that the magnitude and variation in the errors was still acceptable for large organs (e.g. 3 % for the heart and 2 % for the liver) for the 1,5 minute acquisition scan. However for smaller organs the degradation in quantitative accuracy was larger (e.g. 5 % for the kidney and 8 % for the bone marrow). An other study by Slambrouck et al. is olso worth mentioning in the context with this work. They studied the possibility of bias reduction for low statistics Positron Emission Tomography (PET), as the maximum likelihood expectation maximization (ML-EM) reconstruction has a positive bias in regions with low activity [23]. Looking at the result for the ML-EM reconstruction, mean value in hot regions of interest is underestimated, compared to the true mean value, for low count statistics. But for regions with lower activity concentration, the mean value is instead overestimated compared to the true mean value.

The earlier mentioned methods of absorbed dose quantification should still be applicable to the images. Volume of interest (VOI) is defined on CT images, thus the SPECT images do not need to be visually good, however they need to be of high accuracy for quantitative purposes. Thus the task is to lower the acquisition time but still maintain a mean value with low uncertainty. This results in the question formulation: For SPECT imaging, of patients treated with ^{177}Lu-DOTATATE, how much can the acquisition time be reduced when collecting information from 113 keV photopeak and 208 keV photopeak?

2 Theory

2.1 ^{177}Lutetium with DOTATATE

Radionuclide ^{177}Lu is a useful isotope in targeted radionuclide therapy due to its decay scheme, long half life and reliable labeling with biomolecules [16]. It has a half life of 6.65 days and decays with beta emission to the stable isotope, hafnium. The beta emission induces the therapeutic effect and the most commonly occurring beta emission (79.3 %) has a Q-value of 498.3 keV [14] [24], with mean energy of about 149 keV [24]. The gamma emissions creates the possibility to image the radioisotope with a SPECT system. Two of its gamma emissions are of interest for image acquisition, 113 keV with a yield of 6 % and 208 keV

with a yield of 10 % [14] [24]. All of its six known gamma emissions are in the energy interval 72 keV to 321 keV , but the four not mentioned has a yield below 1 % [14] [24] and are therefore not suitable for image acquisition. The decay scheme of ^{177}Lu is presented in figure 1.

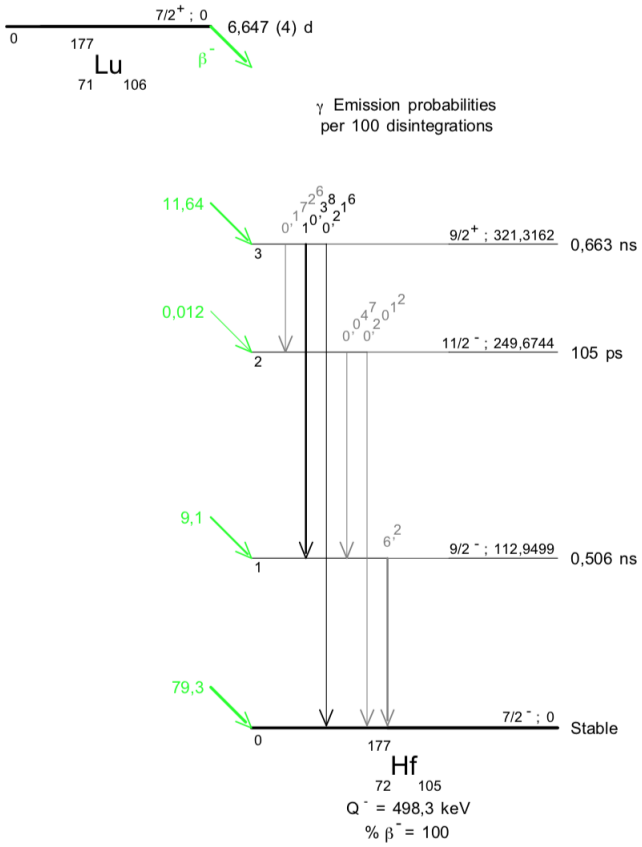

Figure 1: *Decay scheme of* ^{177}*Lu. Image from Table de Radionucléides, LNHB [14].*

A number of peptides can be labelled with ^{177}Lu for different therapeutic purposes [22]. For targeted radionuclide therapy of neuroendocrine tumours, a somatostatin analog octreotate, in this case a peptide called TATE, is labelled with ^{177}Lu by the help of the chelate DOTA , giving the radiopharmaceutical ^{177}Lu-DOTATATE [22] [21]. The somatostatin analog octreotate targets the somatostatin receptors, which are present in high amount on the cell surface of the neuroendocrine tumours and as the radioisotope ^{177}Lu decays the tumour tissue can be damaged [4].

2.2 The Scintillation Camera

The scintillation camera is simply speaking a large scintillation detector used for image acquisition of patients treated or examined with some sort of radiopharmaceutical. The scintillation detector uses the emission of scintillation light to detect the emitted radiation. In the crystal the electrons are arranged in a valance and conduction band, which are different energy levels within the crystal. The energy difference between the valance band and conduction band is called the band gap and is typically about 4 eV. As the crystal is exposed to radiation, the system can, if sufficient energy is added, be excited as electrons move from the valance band to the conduction band. As the system deexcite, electrons move from the conduction band and scintillation light are emitted. To eliminate self absorption of the scintillation light the crystal is introduced with impurities. One example is sodium iodide crystal (NaI) doped with thallium (Tl), which has energy states in between the band gap of the NaI crystal. The electrons will move to the conduction band and before the system deexcites move to the energy state of the Tl. As the system deexcites the electrons move to the

valance band and emitting energy in the form of scintillation light, which are detected in the photomultiplier tube [15].

The SPECT system usually consists of two detector heads, usually placed opposite each other. In order to acquire a three dimensional image the two detector heads moves around the patient, detecting photons in different angles around the patient. All the information collected in a given angle is called a projection. For every angle the detector acquire information from the photons for a set period of time called time per projection. All the counts in a row of pixels, in each projection, are integrated over the vertical axis and the resulting integration from all projections are put together in a sinogram, where the horizontal axis signify the projection bin and the vertical axis the projection angle. The sinogram will be used by the reconstruction algorithm to construct the image. There are several methods to reconstruct an image e.g. analytical and iterative reconstructions [12]. An iterative reconstruction algorithm is used in this study and it is explained in section 2.3.

Seen from the patient perspective, before the scintillation crystal, there is a collimator, which determines which of the photons emitted from the patient that can pass trough to the crystal. The collimator is designed to only let trough photons incident of a certain angle in order to get a spatial dependency in the image [11].

Connected to the detector crystal are a number of photomultiplier tubes, which converts the light signal to a measurable electric signal. The photomultiplier tube consists of three main compartments, the photocathode, dynodes and the anode. The photocathode is a photo-emissive surface with low work function and weakly bound valance electrons. As the photocathode is struck by the scintillation light, it will interact with the photocathode by the photoelectric effect and photoelectrons will be emitted. The material of the photocathode has to emit electrons when incident by the equivalent light quanta of the crystal, for example the NaI(Tl)-crystal emits scintillation light of 415 nm [11].

The photoelectrons are accelerated through a series of dynodes by high potential difference between each dynode. The potential difference accelerates the electrons to the next dynode in the series and as they collides with the dynode more electrons are released through secondary emission. At last the electrons are collected at the anode, where the cascade of electrons are converted to an output current proportional to the incident signal of the scintillation light. Multiple photomultiplier tubes are connected to the scintillation crystal in order to get positioned dependence of the interaction in the detector crystal for every detected event. Based on the magnitude of the output signal form each photomultiplier, for a given interaction, it is possible to determine where the interaction in the crystal originated [11].

The output signal is then matched, shaped and amplified by the preamplifier. Matching of the signal is with respect to the impedance, which is too high for the following compartments of the circuit. The signal has to have a specific decrease time to be properly detected by the amplifier, thus the preamplifier shapes the signal. If needed the signal is amplified. The amount of amplification required varies between the type of detector and the magnitude of the signal. Output signal from the preamplifier is a slowly decaying pulse and results in pulse pileup, which is resolved by the amplifier. The pulse is amplified and shaped by eliminating the tail of the signal, resulting in signals with separate width and no pile up. The amplifier ensures stability between the pulse height and the deposited photon energy in the crystal [11].

Following the amplifier is the multi channel analyser, which sorts the the pulse in different channels depending on the amplitude of the pulse. Amplitude of the pulse is proportional to the deposited energy in the crystal. A lower and higher energy limit can be set to create an energy interval around the photo peak, so called the photopeak window. Only pulses with amplitude within the photopeak window will provide information for the projection in question [11].

2.3 Image Reconstruction

The reconstruction algorithm used in this study is Ordered Subset Expectation Maximization (OS-EM), which is a statistical iterative reconstruction method. The aim of the reconstruction algorithm is to solve the system $P = \mathbf{A}f$, where P are the measured projections, $\mathbf{A}$ is called the system matrix and f is the estimated activity distribution in the image. The system matrix, $\mathbf{A}$, consists of coefficients a_{ij} that provides information of the probability of detecting photons, in a certain bin, emitted from a particular position. Thus

equation 1 gives the expected measured value in a projection bin i from a photon emitted in a pixel j.

$$p_i = \Sigma_j a_{ij} f_i. \tag{1}$$

In the system matrix limitations of the SPECT system e.g. spatial resolution are accounted for, as well as the phenomena of scatter and attenuation. Thus as the reconstruction algorithm solves equation 1 phenomena degrading the image are corrected for. The reconstruction assumes that the signal is homogeneous over the area of the pixel [12].

The OS-EM algorithm is the accelerated version of ML-EM algorithm. Both reconstructions are based on maximizing the so called likelihood objective function (LOF), i.e. finding the reconstructed image f that will with the highest likelihood produce the count distribution of the measured projections P. The likelihood objective function (LOF) is based on Poisson statistics, which maintains positive pixels values and describes the statistics of photon detection. The LOF equation is presented in equation 2, where p is the measured projection, f is estimated activity distribution in the image and $q_i^k = \Sigma_j a_{ij} f_j^k$ are the projections of f, where a_{ij} is a coefficient of the system matrix [12].

$$L(p \mid f^k) = Pr[p \mid f^k] = \Pi_i e^{-q_i^k} \frac{(q_i^k)^{p_i}}{p_i!}. \tag{2}$$

The difference between the two reconstruction methods are how many projections that are used for each update. The ML-EM algorithm uses all projections for every update, i.e. the number of updates are equal to the number of iterations. The OS-EM algorithm only uses a subset of all projections for each update, i.e. the number of updates are greater than the number of iterations. The equation for the ML-EM algorithm is presented in equation 3 [12]. Explained in words the initial guess, f_j^0, of the estimated image is multiplied with the backprojected ratio between the measured projection, p_i, and the estimated projection, q_j^0, to generate the new estimation, f_j^1, which then is used to generate a new estimation and so on. The LOF will increase with every iteration and when the probability of the image f reproducing the measured projection data p, is high enough the resulting image f_j^k is given [12].

$$f_j^{k+1} = \frac{f_j^k}{\Sigma_i a_{ij}} \left[\Sigma_i a_{ij} \frac{p_i}{q_i^k} \right]. \tag{3}$$

As mentioned the difference between the ML-EM and OS-EM algorithm are the number of updates for each iteration. Projections are divided into subsets and for every subset the image data are updated, but the full iteration takes place first when all subsets are used. Performing multiple updates per iteration gives the OS-EM algorithm its accelerating properties compared to the ML-EM algorithm [12]. The acceleration factor of the convergence is proportional to the number of subsets [8].

2.4 Noise

By definition, noise are unwanted fluctuations in the signal which are accumulated together with the signal. Noise arises from the stochastic nature in processes as photon interaction, statistical variations in the detection ability of the detector and electronic noise. The noise level in the reconstructed image will also depend on the iterative reconstruction algorithm, but the noise in itself are originated from the projection data, thus it is not discussed under the topic of noise but instead under section 2.4.2. The noise in SPECT projection images follows a Poisson distribution [17] given by [13], [19], [2]

$$P(x) = \frac{\lambda^x e^{-\lambda}}{x!}, \tag{4}$$

where x are the number of counts and λ is the mean value of counts. From the Binomial distribution the mean value, λ is known to be equal to pn, where p is the individual success probability and n is the number of trials. In the case of decaying nuclei the mean number of counts can also be expressed as $\lambda = At$, where A is the activity and the time t. For low success probability, p, for every trial, n, the binomial distribution

reduces to the form of the Poisson distribution and as this is the case for nuclear medicine imaging the property of λ can be used to derive the variance of the distribution according to equation 5. which is given by

$$\sigma^2 = \Sigma_{x=0}^{\infty}(x-\lambda)^2 P(x) = pn \;\; \Rightarrow \;\; \sigma^2 = \lambda. \tag{5}$$

The standard deviation (SD), σ, of the distribution thus becomes,

$$\sigma = \sqrt{\lambda}. \tag{6}$$

To compare different data sets the fractional standard deviation can be used, which is calculated according to equation 7 [19]. A greater value of fractional standard deviation indicates a larger spread of the data around the mean value.

$$\sigma_F = \frac{\sigma}{\lambda}. \tag{7}$$

Noise in an image can be viewed from different perspectives. From a diagnostic point of view noise are seen in the image as grains covering an area, which, if the detection process were noise free, should have a uniform distribution of counts. The quantitative point of view considers noise as the inability to reproduce the same result from multiple measurements due to processes of stochastic nature. These processes being the radionuclide decay, the photon fluence, the detection process and noise in the electronics [19].

During the image acquisition the number of decays are random from one image acquisition to another. The number of decays with the desirable properties will vary between measurements. Every nuclide has the same probability for decay, which is independent of the other nuclides, meaning that the probability of decay follows a Poisson distribution, equation 4 [2]. Due to the randomness of the disintegration, the amount of decays may deviate between measurements, thus all measurements will not have detected the same amount of counts [19].

The variation in the number of photons incident on the detector, for different measurements, arises from the stochastic nature of photon interaction in material. Distribution of scattered and attenuated photons will vary between measurements, but it has a deterministic mean value, which provides possibilities to correct the image data with respect to the mean value of the distribution. However the distribution around the mean value will vary between measurements and can not completely be accounted for in the correction, thus leaving noise originated from scattered photons and loss of signal due to attenuated photons.

For every incident photon a number of processes will affect the detectors detection ability of the photon. Considering photons of the same energy and a photoelectric interaction in the detector, the number of electrons moving from the valance band to the conduction band will vary among the events. For the same amount of electrons moving the the conduction band, the intensity of the scintillation light will vary as the electrons move back to the valance band. The same reasoning is true for the number of created electrons at the photo cathode, the amplification of the number of electrons in the photo multiplier tube and the how the signal is collected to a charge signal at the anode. All these processes have a random component associated with them, giving rise to an inherent variation from one measurement to another. The nature of these processes leads to the limited energy resolution in a gamma camera-system, which will affect the accuracy of the positioning of the counts in the image. The count position is determined by $\overline{x}_{count} = \frac{\sum_i x_i E_i}{\sum_i E_i}$, where x is the position of the i:th photo multiplier tube and E is the energy detected in the i:th photo multiplier tube. Since the detected energy is affected by the parameters just mentioned, the error will propagate through the count positioning process [3]. The effect limits the spatial resolution, a randomness worth mentioning but will not be studied further in this study.

Noise in the electronics arise from statistical fluctuations as the charge carriers move in the circuit. The amount of electronic noise vary for different hardware and between measurements. Signal from electronic noise will be collected together with the signal originating from the photons [20].

The number of counts detected in every pixel are subjected to random errors, caused by the parameters

discussed above. As the number of counts per pixel increases the mean value increases and according to equation 6 the standard deviation will increase. However, the fractional standard deviation (equation 7) will decrease. Higher accumulated counts will provide less noise in the image [19]. Leaving the conclusion that longer measurement times or higher administrated activity, if not considering dead time, results in improved image quality.

2.5 Image Acquisition & Reconstruction effects on image noise

As the acquisition time is decreased the signal to noise ratio (SNR) will decrease. There are several factors affecting the noise level in an image.

2.5.1 Image Acquisition

For the image acquisition a number of parameters affect the quality of the image. They are the number of projection angles, the acquisition time per projection, the matrix size, the energy window, the collimator and count rate problems.

The number of projection angles can affect the SNR in the reconstructed image, but it has to be considered together with the time per projection. If the total acquisition time remains the same, the number of projection angles should not affect the noise level in the reconstructed image, since the SNR remains the same. For the same time per projection and less projection angles, thus decreasing the total acquisition time, the SNR in each projection will remain but the noise level in the reconstructed image will increase due to lost signal for every projection angle not measured.

Time per projection affects the SNR in the image. A decrease in time per projection results in a lower SNR. The mean counts in each projection will decrease, thus the fractional SD, equation 7, will increase. For the same reason the pixel size affect the SNR, considering the mean counts per pixel. When the size of the matrix increases the SNR decreases, as the pixels becomes smaller. Pixels in an 256×256-matrix will cover an area four times smaller than pixels in an 128×128-matrix, thus detecting four times less counts in each pixel. For the same acquisition time the SNR in each pixel will be worsen with a factor 2 in the 256×256-matrix, relative the 128×128-matrix. Considering also a change in the third dimension, the slice thickness, the SNR will worsen with a factor $\sqrt{8}$ for the $256\times256\times256$-matrix [17].

The size of the energy window of the full absorption peak will affect the SNR in the image. Due to the limited energy resolution in the scintillation crystal an energy interval around the desired photon energy has to be accepted as a full absorbed event. Typically the energy window is 15-20 % around the photon energy. Considering a detector with perfect energy resolution, the full absorption peak would be detected as a delta function, equal to the photon energy, but as seen in figure 2 it has a width. The limitation determines the lower energy threshold of the energy window, which introduces scatted photons to be detected in the energy window. A system with better resolution will only result in less scattered photons in the energy window if it is narrowed. Comparing SPECT systems with 7 % energy resolution and 12 % energy resolution, both will accept as much scatter in the energy window if the same lower energy threshold is set [3].

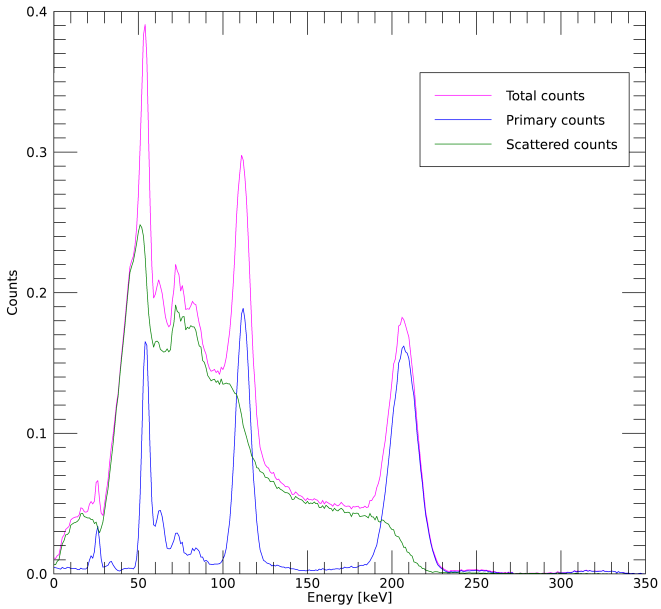

Figure 2: *Spectrum of Lu-177, simulated with SIMIND.*

The collimation has both positive and negative properties to the image acquisition. Without it there would be no position resolution in the image, but with it there is a loss in sensitivity of the imaging system [3]. Because of the loss of counts, due to the collimator, the SNR in the image will decrease.

Count rate issues in systems resulting with dead time can be explained either by, non-paralysable or paralysable dead time. The non-paralysable dead time effect occurs when an event causes the system to be unresponsive for the following events during a period of time. The paralysable dead time occurs when following events prolongs the unresponsive time of the system [3]. Dead time results in a loss of counts, thus a greater statistical uncertainty in the image. For count rates where dead time is a problem it has to be corrected for.

2.5.2 Reconstruction

The iterative reconstruction method ordered subset expectation maximization (OS-EM) is used in this study. The reconstruction process includes parameters such as number of iterations, number of subsets, correction parameters and filtering.

The number of iterations affects the noise level in the image. Every iteration will amplify the noise level [2]. There is no exact criterion to determine the number of iterations to use in the clinic. One way to optimize the number of iterations are based on convergence of the recovery coefficients, which usually are determined from experiments, for instance by use of phantom studies in a geometry representative of a patient. The recovery coefficients are calculated by dividing the measured activity by the true activity [10]. The coefficients are evaluated for every iteration and the number of iterations are chosen based on the convergence behaviour of the recovery coefficients.

For a large number of subsets and projections with high noise level, the OS-EM algorithm, compared to the ML-EM algorithm, does not have as good noise properties [8]. For every subset, the data are updated, meaning that for each update the data treated are changing. It is reasonable to assume that a larger number of angles per subset (i.e. fewer subsets) will improve the stability against noise, since then there are more

counts in total, that are back-projected for each subset. However, this becomes a trade off with the convergence speed, which becomes slower with a decreasing number of subsets.

To reduce noise level the data can be filtered to suppress some frequencies. Since the data in this study are used for quantitative purposes no filtering is done. Filtering data has a tendency to change the distribution of counts in the image, thus should only be used for visual improvement [12].

2.5.2.1 Correction parameters During and post reconstruction a number of corrections of the data are performed. Correction for scatter, attenuation and collimation are performed during with the reconstruction. Partial Volume effect (PVE) and dead time are corrected for post reconstruction.

Scatter correction compensates for photons scattered between the point of emission and the detector and are detected in the energy window of the full absorption peak. The detected scattered events lead to degradation in contrast and activity quantification and thus must be corrected for [2]. The scatter correction used is Effective Scatter Source Estimation (ESSE), which estimates the scatter in the energy window with scatter kernels obtained from Monte Carlo (MC) simulation [16]. The correction in itself is not expected to contribute to noise in the image, but if the image has a high noise level it may affect the quality of ESSE correction. However this effect is believed to be very small. In clinical practice other methods for scatter correction is typically used, e.g. triple energy window correction [2].

Attenuation of photons between the point of emission and the detector reduces the photon fluence and in turn information for the image. To account for this loss a low dose CT of the patient is transformed from hounsfield units (HU) to a map of mass attenuation coefficients, μ-values, for the administered radionuclide. Noise in the CT image will propagate to the SPECT image and if the same CT image is used for the attenuation correction the error will be systematic, thus introducing the same amount of noise in all the SPECT images. For this study this is the case, but in patient images the noise level in the CT image will vary between patients and so will also the noise propagating to the SPECT image.

Collimator Response Function Compensation (CRFC) is performed to compensate the limitation of the spatial resolution caused by the collimator, as discussed in section 2.5.1. The spatial resolution of a SPECT system is distant dependent and if not corrected for the resolution will decrease with the distance from the collimator, but if CRFC is performed the resolution in the reconstructed image becomes approximately the same over the FOV. Spatial resolution of the system is usually modelled as a Gaussian function, which mimics the smear of a point source as a function of distance from the collimator. The source distribution is convolved with the distance dependent Gaussian function to correct for the smear out [2]. The correction changes the texture of the noise in the images. It tends to increase the noise level in the middle frequencies resulting in a ”blobby” noise texture [2], also called the smoothing effect.

Partial volume correction (PVC) compensates for the spillover effect and the finite size of voxels [3]. The spillover effect is due to the limited spatial resolution in a SPECT system. A point source will, by the SPECT system, be approximated as a Gaussian function, meaning that for example a small sphere filled with activity will have a larger diameter in the image compared to its true diameter [2]. This is due to the spillover effect, i.e. partial volume effect, and the finite size of voxels that result in a limitation to accurately reproduce the activity distribution. Partial volume correction is complicated, due to the unbalanced spillover effects in different regions, it is hard to model. The effect varies with the size and shape of the object, the activity distribution and objects and activity in the surrounding background [3]. Typically PVC is based on phantom measurement and estimation of recovery coefficient, where the recovery coefficient is a function of object size, object shape, activity concentration and position in the image, thus the uncertainty in the PVC will be systematic in all SPECT images. Note that there is a number of other ways to correct for the partial volume effect [2].

Dead time is not an issue for ^{177}Lu treatments with injection activity of 7400 MBq, thus it is not corrected

for [16].

2.6 Monte Carlo Simulations with SIMIND

The Monte Carlo code SIMIND simulates a SPECT system. Simulations of projection data from SIMIND corresponds to projection data that could be acquired from measurement with substantial SPECT system with hardware and software [7]. All the physical processes involved in the measurement are modelled with probability density functions (pdfs). Monte Carlo methods simulate the reality by random sampling from the pdfs. To obtain accurate results a large amount of particle histories, must be simulated. The pdfs describe every process from how the isotope decays, how the particles interact in the phantom, photons passage in the collimator and to the detection in the scintillation crystal [1].

3 Method

3.1 Simulation & Reconstruction

Monte Carlo code SIMIND was used to simulate the projections of a cylindrical phantom, within it six spheres with different volumes (se table 2). To simplify the possibility to alter the activity concentration in the spheres and background of the phantom independent of each other, two projection sets were simulated. One projection set contained activity in the spheres and a cold background and one set contained cold spheres and activity in the background. For both projection sets the total activity in the phantom was 1 MBq and the activity was homogeneously distributed over the source regions. Thus resulting in the same activity concentration in all six spheres and a homogeneous background activity in the background simulation. 100 million histories were simulated per projection and the detector was set 2 cm from the edge of the phantom. Time per projection was 1 second and 60 projection angles. Projection data of energy window of 208 keV and 113 keV were simulated in separate projection sets. For each photon energy the energy window was centred around the photopeak, i.e. for 208 keV$\pm$7.5 % and 113 keV$\pm$10 %.

To mimic projection data acquired with different time per projection, the projection data of the spheres as hot spots, were multiplied with values, named Disintegration Concentration value (DC-value)[MBq·s/ml], to obtain different disintegration concentrations in the spheres. Higher disintegration concentration signify longer time per projection because of the increase in detected counts and lower disintegration concentration indicates a shorter time per projection due to less detected counts. Typical activity concentration in kidney and tumours respectively, approximately 96 h after injection, were derived from SPECT images of 5 patients. Results for kidney: 0.22 $\pm$ 0.06 MBq/ml and tumours: 1 $\pm$ 0.8 MBq/ml. Time per projections from 45 seconds/projection, according to today's image protocol, and down to time per projection of 7.5 seconds/projection were tested. With respect to the limitation in the cameras rotation speed, time per projection shorter than 7.5 seconds was not believed to be of interest. However based on a study by He and Frey, even shorter time per projection is needed to reach the level where the noise becomes the dominant error factor [6]. Thus DC-values corresponding to very short time per projection were evaluated to make sure that the point where the reconstructed images would no longer be acceptable for absorbed dose quantification would be found. Deriving the largest Disintegration Concentration value by multiplying the the observed activity concentration in tumours (1 MBq) with the highest time per projection (45 seconds) giving DC-value=45 MBq·s/ml. By lowering the DC-value in steps of DC-value$\times$0.5 and deciding to test 10 different times per projection the DC-value becomes a vector of 10 elements, presented in table 1. The DC-values are converted to time per projection by dividing it with the activity concentration observed from patients images. For kidneys the DC-value were divided by the mean value of the activity concentration subtracted with two standard deviations (DC-value/(0.22-2$\times$0.06 MBq/ml)), to also include kidneys with low activity concentration 96 h p.i. For tumours the DC-values were divided with the mean value of the activity concentration (DC-value/(1 MBq/ml)).

Table 1: *Disintegration Concentration value and the corresponding time per projection for tumours and kidneys respectively.*

DC-value [MBq·s/ml]	Time per projection tumour [s]	Time per projection kidney [s]
45.00	45.00	450.00
22.50	22.50	225.00
11.25	11.25	112.50
5.625	5.63	56.25
2.81250	2.81	28.13
1.40625	1.41	14.06
0.703125	0.70	7.03
0.351563	0.35	3.52
0.175781	0.18	1.76
0.0878906	0.09	0.88

To evaluate the effect of different contrasts, in disintegration concentration, between the spheres and the background, the projection set with activity in the background were multiplied with a value to obtain four contrasts relations sphere-to-background, C_{sphere}:C_{bkg}=10:1, 7:1, 4:1 and 1:0. The contrast in patient images acquired 96 h p.i. was evaluated by placing ROIs inside and outside tumors and kidneys, and values of approximately 7:1 were obtained. Projection sets multiplied with DC-values to change disintegration concentration in the spheres were combined with the different C_{sphere}:C_{bkg}, giving a total of 40 new projection sets per energy window. Noise were added to the projections with the IDL-function *Poidev* and for each projection set, 50 noise realisations were created to get an acceptable low statistical fluctuation in the mean value, giving a total of 4000 projections, including both energy windows. The schematic creation of the projection sets are presented in figure 3.

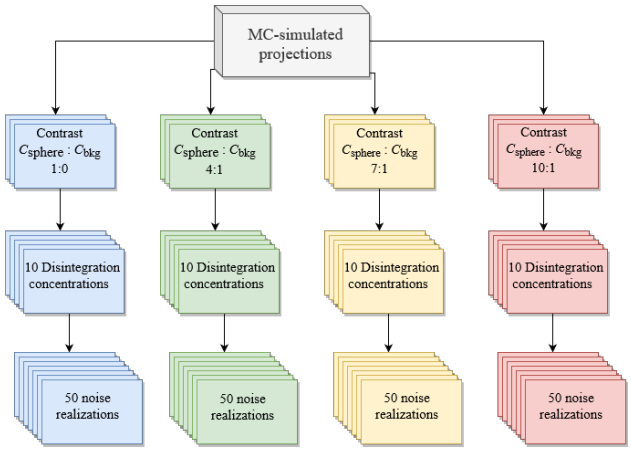

Figure 3: *Schematic overview of the created projection sets. This were done for 113 and 208 keV respectively.*

The projection sets were reconstructed using the reconstruction model in the in-house dosimetry package LundADose [18], using OS-EM with 6 subsets and 40 iterations. Number of iterations were determined by evaluating the convergence of the recovery coefficients as a function of iteration. For every iteration from 1 to a 100 the resulting reconstructed images were saved and by applying created masks of the spheres (se section 3.2) to the images, recovery coefficients were calculated. The recovery coefficients for each sphere were plotted as a function of iteration and the number of iterations were chosen based on where the recovery, for all the spheres had converged. Due to the large number of projection data with different DC-values and C_{sphere}:C_{bkg}, for time conservation purposes, the recovery coefficients were evaluated on noise free projections, for this initial determination of the number of iterations.

The images were corrected for scatter, attenuation and collimator response. Images were converted from counts to becquerel by dividing with the sensitivity of the SPECT system. The reconstructed images had a matrix size of 128×128×128 voxels but was regrided to a 512×512×512-matrix, to simplify the VOI definition.

3.2 Masks

For evaluation of the images, masks of the spheres were created using the three-dimensional spherical equation with the known centrers and radii of the spheres. The initial mask had a matrix size of 128×128×128 voxels, but comparison of the volume of the mask-spheres and the true volume of the spheres deviated too much. For a matrix of smaller voxels, the mask can more correct reproduce the true volume of the spheres. Thus the mask was created for a matrix size of 512×512×512 voxels, giving a deviation in volume of 0.1-0.6 % for the different spheres. To validate the location of the masks, the matrix of the mask was applied on the reconstructed images and the correct position of the mask was validated by visual evaluation.

3.3 Evaluation

For evaluation of the images the mask of the spheres was applied to the reconstructed images. From the images the mean value of the disintegration concentration, $\overline{m}$ [(MBq×s)/voxel], in each sphere was calculated. For the 50 noise realisations, originating from the same projection set, the mean value of all the 50 mean values, for each sphere was calculated. Further the standard deviation (SD) of all the 50 mean values, from every projection set and sphere was calculated, respectively. To compare different data of the projections the coefficient of variation (CV) was used, according to,

$$CV = \frac{s(\overline{m}_{50})}{\overline{m}(\overline{m}_{50})}, \tag{8}$$

where $s(\overline{m}_{50})$ is the standard deviation of the 50 mean values from the 50 noise realisations and $\overline{m}(\overline{m}_{50})$ is the mean value of the 50 mean values from the 50 noise realisations. Evaluation was done for 113 keV, 208 keV and 113+208 keV. To evaluate 113+208 keV corresponding data, out of the aspect of DC-value and contrast C_{sphere}:C_{bkg}, from 113 keV and 208 keV images were summed together. The mean value for 113+208 keV was calculated by arithmetic mean value, by summing up the mean value of the disintegration concentration in each sphere, from 113 keV and 208 keV data, and dividing the sum with a 100 (total number of mean values summed). The standard deviations were calculated from the resulting calculated mean values of 113+208 keV.

To simplify the evaluation the spheres were given names presented in table 2, where the largest sphere simulated the kidney and the five smaller spheres simulated tumours of different sizes. Kidneys are larger but in this case it was the largest volume available. The smallest sphere is a bit too small, lesions of this size are normally not possible to evaluate due to the PVE, thus it was in some cases excluded from the evaluation.

Table 2: *The six spheres in the phantom presented with their evaluation names and their corresponding volumes.*

Sphere number	Name	Volyme [ml]
1	Kidney	59.6
2	Tumour 1	49.3
3	Tumour 2	19.6
4	Tumour 3	16.2
5	Tumour 4	8.0
6	Tumour 5	3.9

The data were plotted for recovery as a function of sphere volume, recovery as a function of DC-value and CV as a function of DC-value, normalized to the measured and true disintegration concentration in the spheres respectively. In order to ensure accuracy in the mean value of the disintegration concentration in the VOI, an acceptance criterion was set to the CV. The dosimetry of kidneys, has in the best case, an uncertainty of 5 % and for the dosimetry of tumour an uncertainty of 10 % [5]. The acceptance criterion to the CV was set to only increase the uncertainty to the dosimetry with maximum 1 %, giving the criterion presented in table 3. For the recovery a similar criteria was set because the result showed a bias dependent on the activity concentration, a bias which would be very hard to correct for. Thus the criteria was set based on the recovery obtained from DC-value=45.00 MBq·s/ml, i.e. the longest time per projection, to make sure that the expectation value of the recovery did not differ too much from the image acquisition conditions with the highest statistical certainty. The criteria for the recovery are also presented in table 3.

Table 3: *The acceptance criterion set to the kidney and the tumours respectively.*

Sphere name	CV criteria	Recovery criteria
Kidney	$\leq$3 %	$\pm$3 % from recovery obtained for DC-value=45.00 MBq·s/ml
Tumour 1-5	$\leq$5 %	$\pm$5 % from recovery obtained for DC-value= 45.00 MBq·s/ml

Based on the acceptance criterion tables for every photon energy and contrast C_{sphere}:C_{bkg} were created to evaluate which spheres fulfilled the criterion for every DC-value.

4 Results

4.1 Recovery as a function of sphere volume

Figure 4-5 presents the recovery as a function of sphere volume for 208 keV for the two of contrasts ratio C_{sphere}:C_{bkg}=1:0 and 7:1. Photon energy 113 keV is presented in figure 6-7 and 113+208 keV is presented in figure 8-9. The recovery is calculated by the mean disintegration concentration in the VOI. The error bars display the error of the mean of the 50 noise realisations divided with the true disintegration concentration. Note that only six of the DC-values are presented and the y-axes are cropped to a certain interval, for visual purposes. Graphs with all DC-values, contrast ratio and unlimited y-axes are presented in appendix A.1.

Generally for all the graphs the recovery is lower for smaller sphere volumes and there is also a larger spread in recovery coefficients between DC-values for the smaller sphere volumes. For 208 keV the variation in recovery coefficients has a larger spread for contrasts with background compared to C_{sphere}:C_{bkg}=1:0. However, this pattern is not visible for 113 keV and 113+208 keV. The graphs presented in the result are limited to the interval [0,1] on the y-axes. The recovery for some data sets fall outside of this interval, having an overestimation of the recovery of hundreds of percent, due to some poorly reconstructed images.

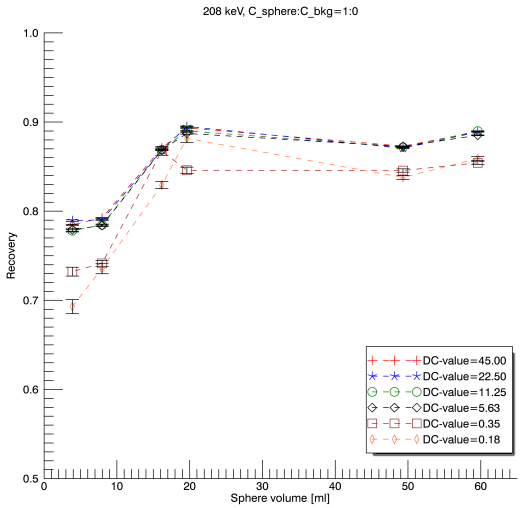

Figure 4: *Recovery as a function of volume of the spheres for 208 keV photons and contrast* C_{sphere}:C_{bkg}*=1:0.*

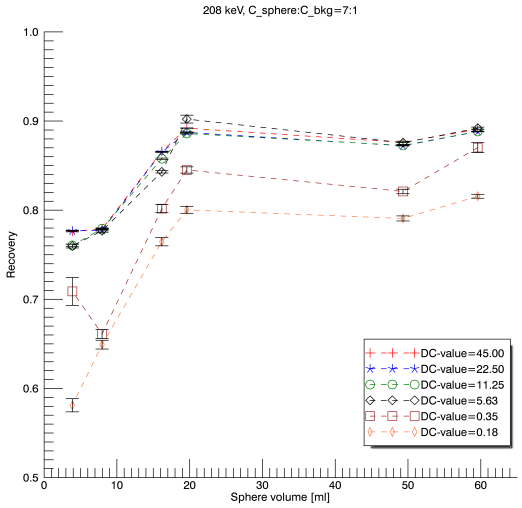

Figure 5: *Recovery as a function of volume of the spheres for 208 keV photons and contrast* C_{sphere}:C_{bkg}*=7:1.*

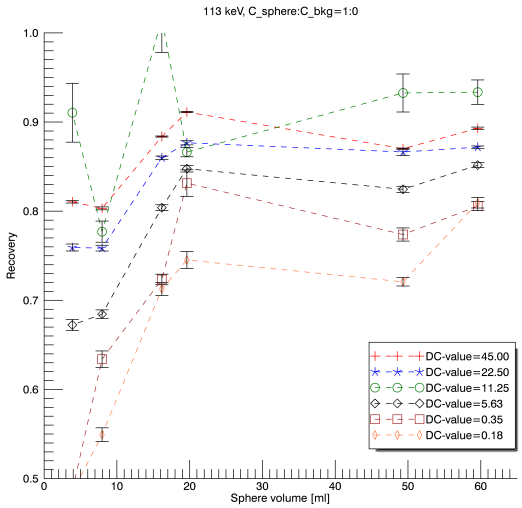

Figure 6: *Recovery as a function of volume of the spheres for 113 keV photons and contrast* C_{sphere}:C_{bkg}*=1:0.*

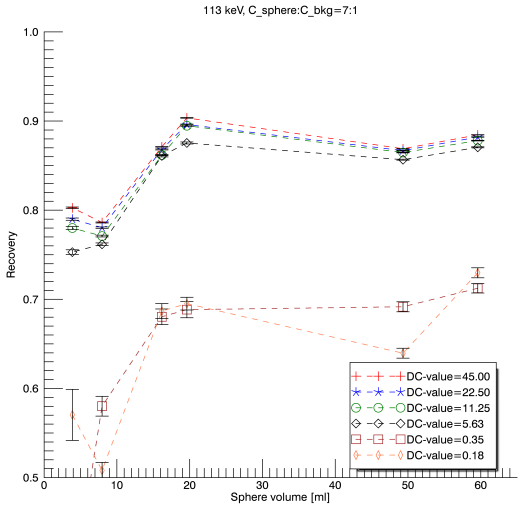

Figure 7: *Recovery as a function of volume of the spheres for 113 keV photons and contrast* C_{sphere}:C_{bkg}*=7:1.*

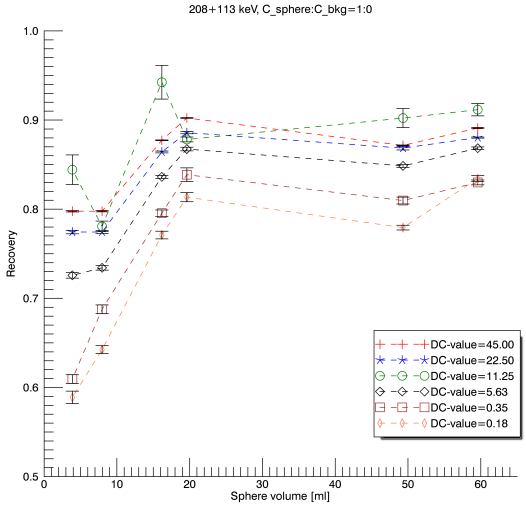

Figure 8: *Recovery as a function of volume of the spheres for 113 and 208 keV photons and contrast C_{sphere}:C_{bkg}=1:0.*

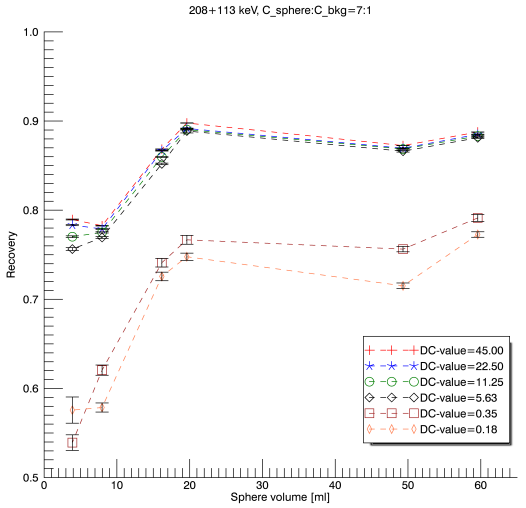

Figure 9: *Recovery as a function of volume of the spheres for 113 and 208 keV photons and contrast C_{sphere}:C_{bkg}=7:1.*

4.2 Recovery as a function of disintegration concentration value

The recovery calculated by the mean disintegration concentration in a VOI is presented as a function of DC-value. Figure 10-11 displays the result for 208 keV, figure 12-13 displays 113 keV and 14-15 displays 113+208 keV. The error bars display the error of the mean of the 50 noise realisations divided with the true disintegration concentration. Only two of the contrasts ratio C_{sphere}:C_{bkg} is presented in the result but the same tendency is seen for all the contrasts. Note that the y-axes are cropped, for visual purposes. The remaining contrast ratio C_{sphere}:C_{bkg} and graphs with unlimited y-axes are presented in appendix A.2.

The graphs all show the same tendency, the recovery is lower for the low DC-values and becomes higher with increase in DC-value. The recovery coefficients are stabilizing around DC-value=11.25 MBq·s/ml and higher DC-values beyond that doesn't improve the recovery to a large extent. As mentioned the y-axes

in the graphs presented in the result are cropped. Due to some poorly reconstructed images resulting in a overestimation of the recovery of hundreds of percent, it became hard to clearly see the interesting interval of the recovery between 0 and 1.

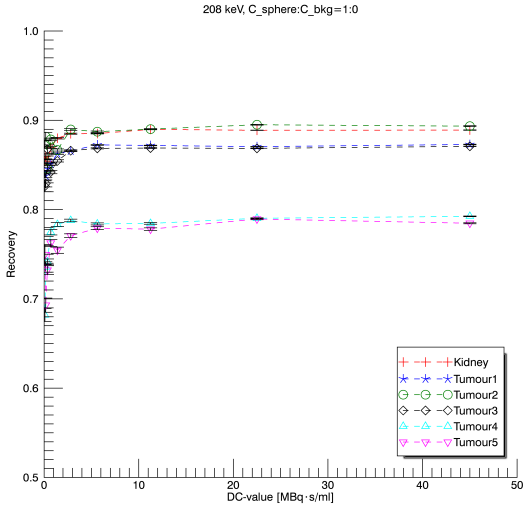

Figure 10: *Recovery as a function of DC-value for 208 keV photons and contrast C_{sphere}:C_{bkg}=1:0.*

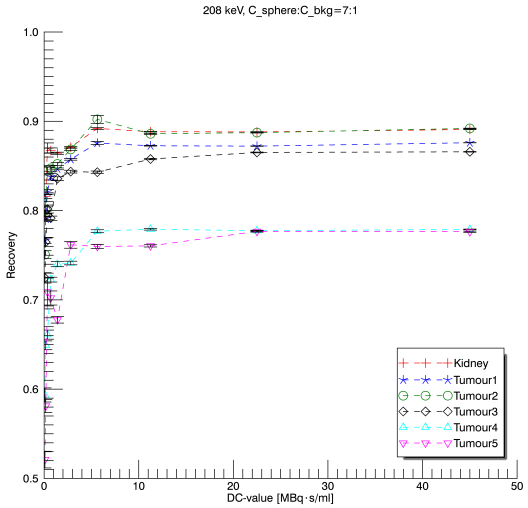

Figure 11: *Recovery as a function of DC-value for 208 keV photons and contrast C_{sphere}:C_{bkg}=7:1.*

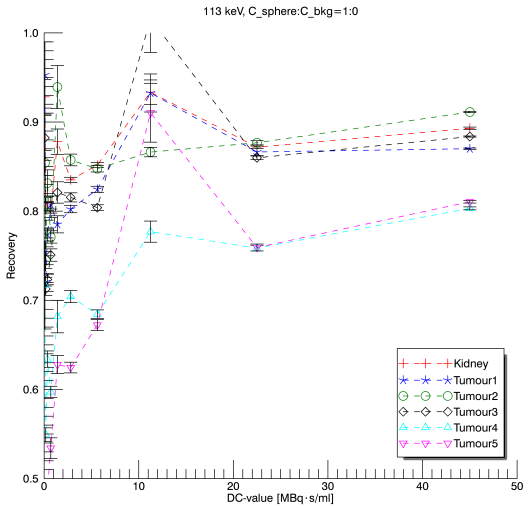

Figure 12: *Recovery as a function of DC-value for 113 keV photons and contrast C_{sphere}:C_{bkg}=1:0.*

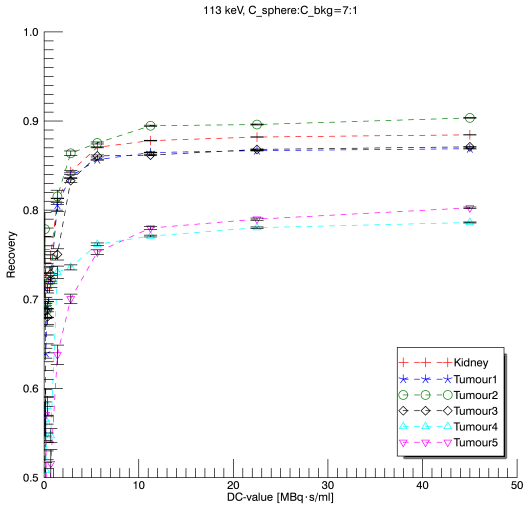

Figure 13: *Recovery as a function of DC-value for 113 keV photons and contrast C_{sphere}:C_{bkg}=7:1.*

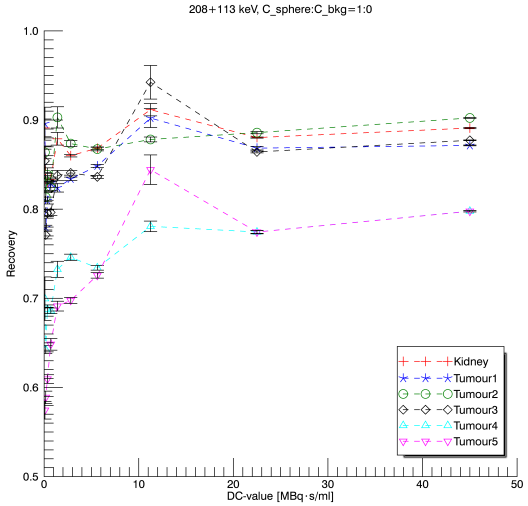

Figure 14: *Recovery as a function of DC-value for 113 and 208 keV photons and contrast C_{sphere}:C_{bkg}=1:0.*

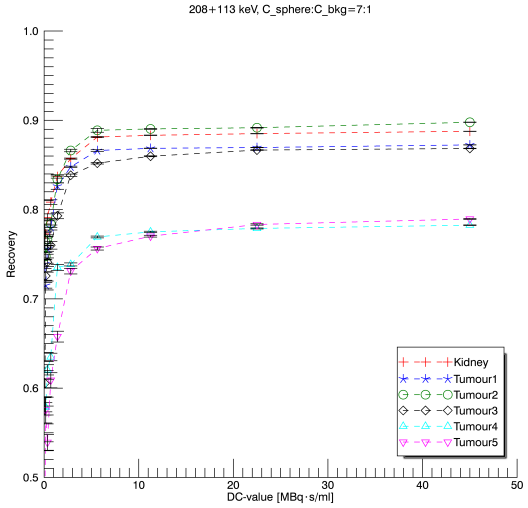

Figure 15: *Recovery as a function of DC-value for 113 and 208 keV photons and contrast C_{sphere}:C_{bkg}=7:1.*

4.3 Coefficient of variation as a function of disintegration concentration value

The following figures display CV, in decimal form, as a function of DC-value. For comparison the standard deviation is both divided with the measured disintegration concentration and true disintegration concentration, respectively. The two graphs, for one photon energy and contrast C_{sphere}:C_{bkg}, are presented next to each other. Figures 16-17 present results for 208 keV, figures 18-19 present result for 113 keV and figures 20-21 present result for 113+208 keV. The acceptance criteria, according to table 3, are displayed by two solid lines, the black being the highest accepted CV for the tumours and the red being the highest accepted for the kidney. Only two of the contrasts ratio C_{sphere}:C_{bkg} is presented in the result but the same tendency is seen for all the contrasts. Note that the y-axes are cropped, for visual purposes. The remaining contrast ratio C_{sphere}:C_{bkg} and graphs with unlimited y-axes are presented in appendix A.3.

For all the graphs CV is higher for lower DC-values and with increasing DC-value CV becomes lower, as a result of a higher noise level in the images. In most cases the lowest CV is seen for the DC-value=45.00

MBq·s/ml. CV did in some data sets reach higher values then presented in the figures in the following section. The axes was cropped for visual purposes, to easily compare the data where the standard deviation is divided with the measured disintegration concentration and the true disintegration concentration. When comparing the two presentations of the data the pattern is the same, however the standard deviation divided with the true disintegration concentration has lower values compared to the standard deviation divided with the measured disintegration concentration.

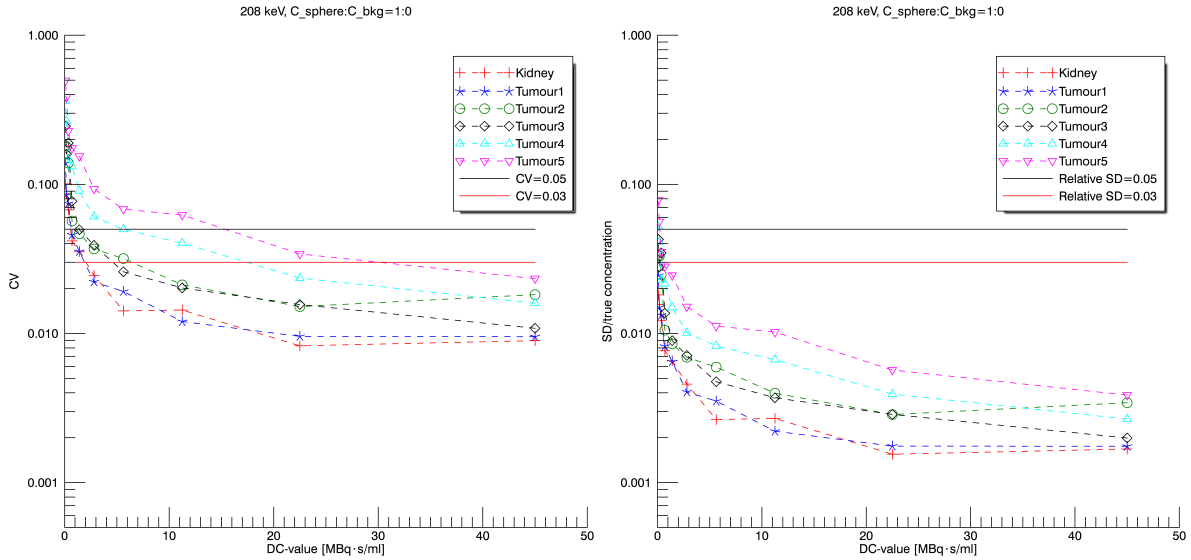

Figure 16: *For 208 keV photons and contrast C_{sphere}:C_{bkg}=1:0. Left graph present CV, standard deviation divided by the measured disintegration concentration in the spheres, as a function of DC-value. Right graph present the standard deviation divided by the true disintegration concentration in the spheres, as a function of DC-value.*

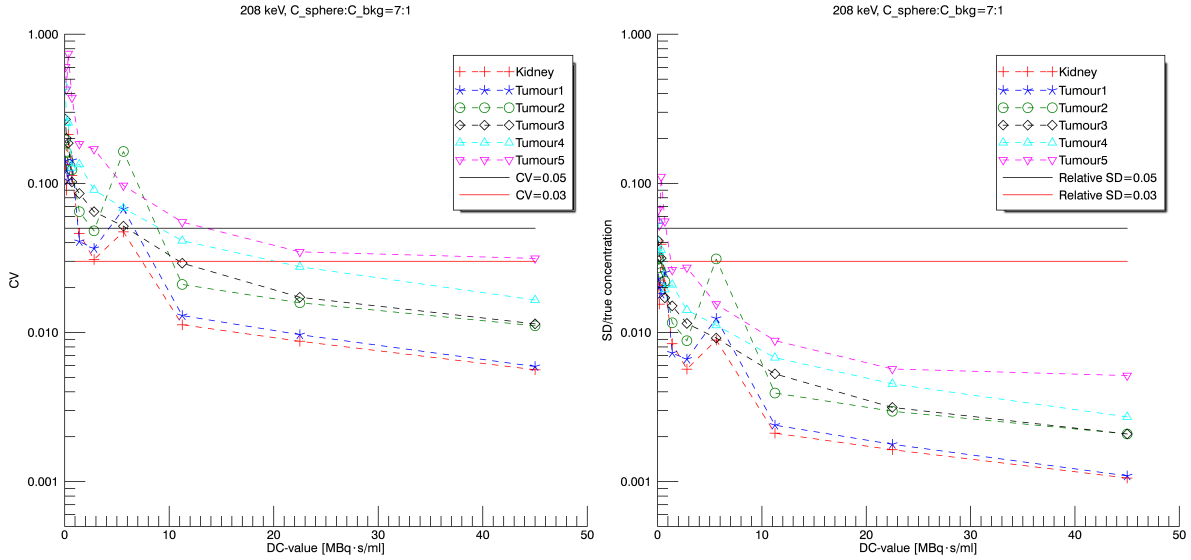

Figure 17: *For 208 keV photons and contrast C_{sphere}:C_{bkg}=7:1.Left graph present CV, standard deviation divided by the measured disintegration concentration in the spheres, as a function of DC-value. Right graph present the standard deviation divided by the true disintegration concentration in the spheres, as a function of DC-value.*

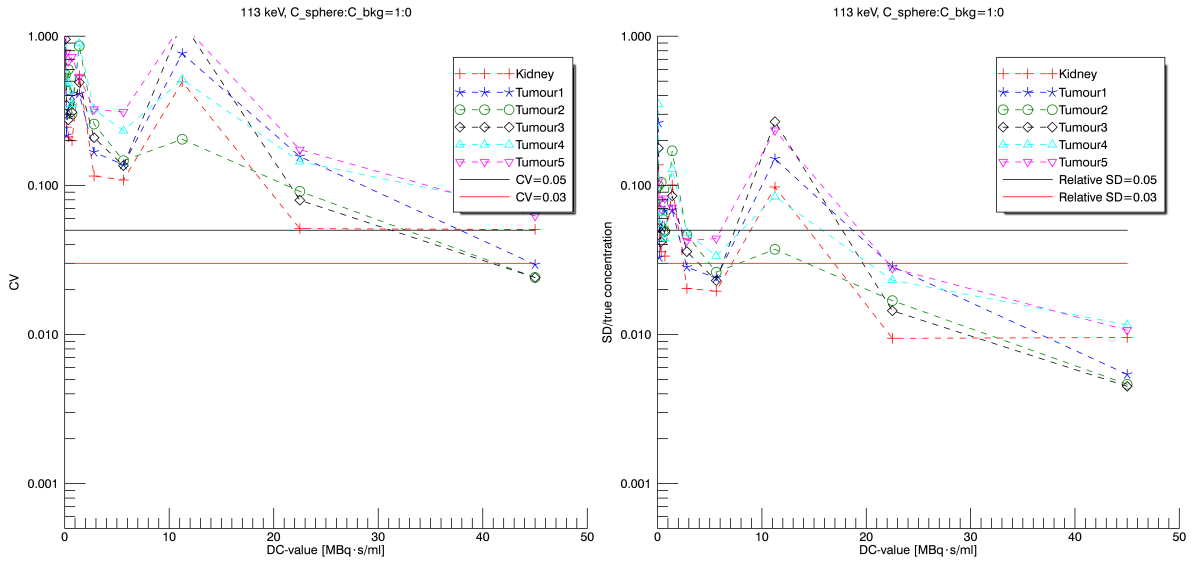

Figure 18: *For 113 keV photons and contrast C_{sphere}:C_{bkg}=1:0. Left graph present CV, standard deviation divided by the measured disintegration concentration in the spheres, as a function of DC-value. Right graph present the standard deviation divided by the true disintegration concentration in the spheres, as a function of DC-value.*

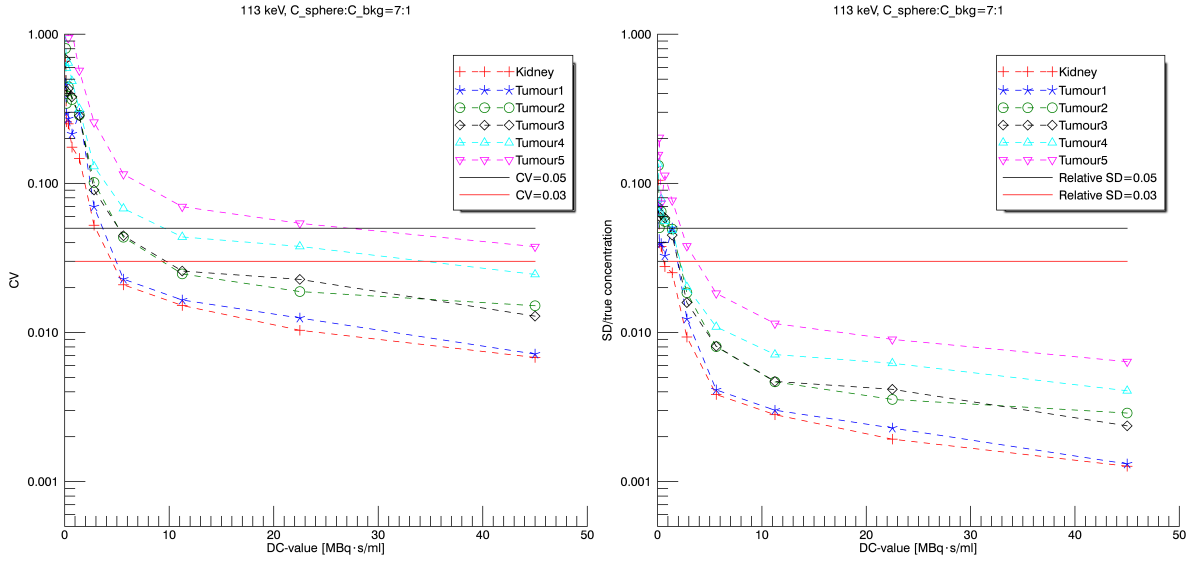

Figure 19: *For 113 keV photons and contrast C_{sphere}:C_{bkg}=7:1. Left graph present CV, standard deviation divided by the measured disintegration concentration in the spheres, as a function of DC-value. Right graph present the standard deviation divided by the true disintegration concentration in the spheres, as a function of DC-value.*

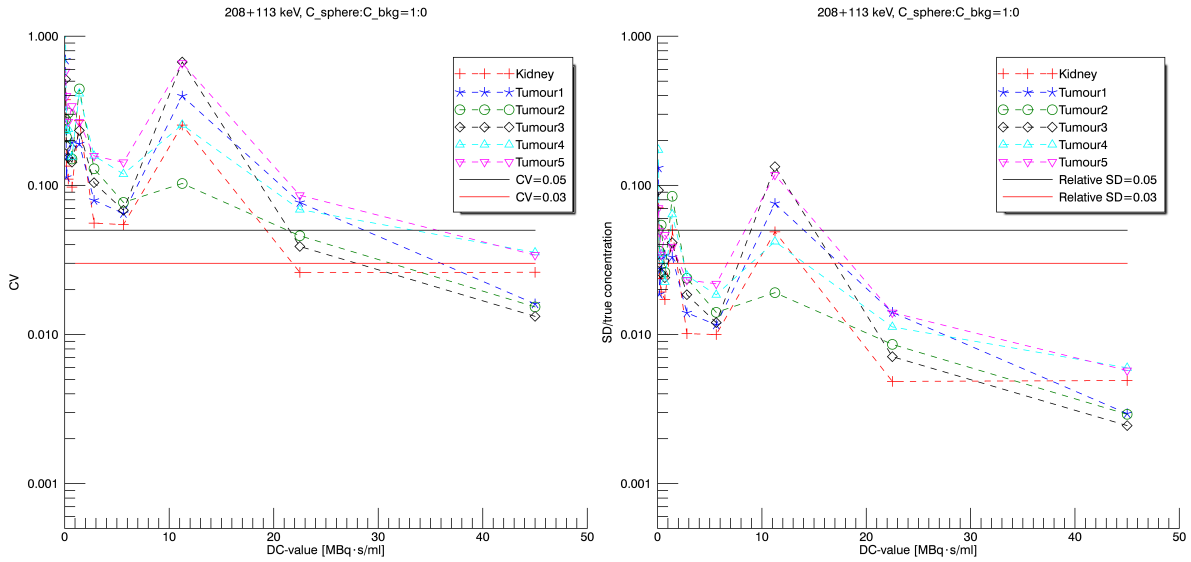

Figure 20: *For 113 and 208 keV photons and contrast C_{sphere}:C_{bkg}=1:0. Left graph present CV, standard deviation divided by the measured disintegration concentration in the spheres, as a function of DC-value. Right graph present the standard deviation divided by the true disintegration concentration in the spheres, as a function of DC-value.*

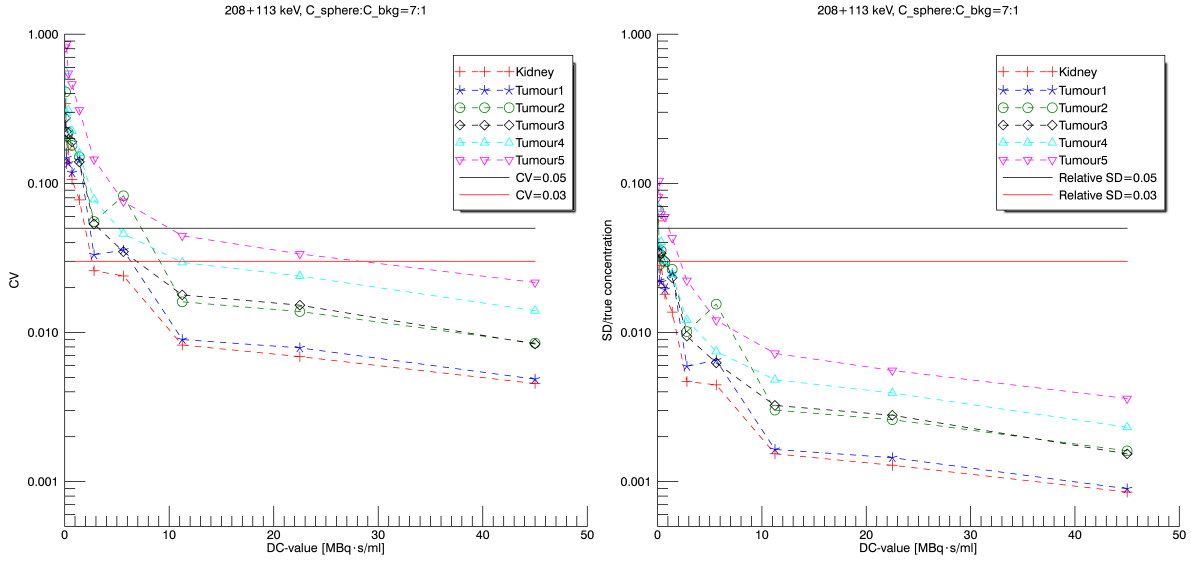

Figure 21: *For 113 and 208 keV photons and contrast C_{sphere}:C_{bkg}=7:1. Left graph present CV, standard deviation divided by the measured disintegration concentration in the spheres, as a function of DC-value. Right graph present the standard deviation divided by the true disintegration concentration in the spheres, as a function of DC-value.*

4.4 Acceptance Criteria

Table 4 presents the lowest DC-value, that fulfils the acceptance criterion in table 3 for every photon energy and contrast C_{sphere}:C_{bkg}. The table summarizes the result of the acceptance criteria presented in appendix A.4.

Excluding the contrast C_{sphere}:C_{bkg}=1:0, the DC-value that all the other contrast levels fulfilled is DC-value=22.50 MBq·s/ml, for all different energy windows. Thus adding a second energy window around the 113 keV photopeak doesn't seem to improve the image out of the aspect of the set acceptance criterion of recovery and CV. DC-value=22.50 MBq·s/ml would, for image acquisition of tumours result in a time

per projection of 22.5 seconds and for kidneys 225 seconds per projection. For projection sets with low disintegration concentration in the background, C_{sphere}:C_{bkg}=1:0 and C_{sphere}:C_{bkg}=10:1, lower DC-values are meet to a lower extent apart from 208 keV, C_{sphere}:C_{bkg}=1:0.

Table 4: *Fulfilment of acceptance criterion for both photon energies and combined, with all four contrast levels.*

Energy Window & C_{sphere}:C_{bkg}	Fulfills criterion
208 keV, 1:0	DC-value=5.63 MBq·s/ml
208 keV, 10:1	DC-value=22.50 MBq·s/ml
208 keV, 7:1	DC-value=11.25 MBq·s/ml
208 keV, 4:1	DC-value=11.25 MBq·s/ml
113 keV, 1:0	None
113 keV, 10:1	DC-value=11.25 MBq·s/ml
113 keV, 7:1	DC-value=11.25 MBq·s/ml
113 keV, 4:1	DC-value=22.50 MBq·s/ml
208+113 keV, 1:0	DC-value=45.00 MBq·s/ml
208+113 keV, 10:1	DC-value=22.50 MBq·s/ml
208+113 keV, 7:1	DC-value=11.25 MBq·s/ml
208+113 keV, 4:1	DC-value=45.00 MBq·s/ml

5 Discussion

5.1 Recovery as a function of sphere volume

Studying the result presented in figure 4-9, the pattern is the same for both photon energies and the combined. As expected the recovery are not as good for the smaller volumes compared to the larger volumes. For smaller volumes, a larger fraction of voxels will border to the background. Hence, the signal reduction due to spillover effects will be more prominent, resulting in a lower recovery. The recovery has a larger variation for the shorter time per projections compared to longer time per projection. However for DC-values= 45.00-5.63 MBq·s/ml the recovery are much more stable, indicating that longer time per projection, beyond DC-value=5.63 MBq·s/ml , does not improve the recovery. The disintegration concentration is to a larger degree underestimated for shorter time per projections.

In some cases the recovery reached unreasonable values, overestimating the disintegration concentration from a few percent up to hundreds of percent. Note that the graphs shown in section 4 has limited y-axes, so these unrealistic result are not seen. The uncut graphs are instead shown in appendix A.1, figure 22-33. The origin of the high recovery are high total and max values in some noise realisations compared to the 50 other noise realisations with the same conditions. It is believed to be a result of high resulting values as the measured projection is divided with the estimated projection in the reconstruction algorithm, equation 3. These poor reconstructed noise realisations are more frequently seen for lower time per projection and low background, i.e. for low amount of total counts. Dividing with very small values leads to high resulting values, thus giving rise to the high pixel values in the reconstructed image. Since the amount of noise realisations were quite small, the mean value of the 50 noise realisations are sensitive to deviation in between the reconstructions. If a larger amount of noise realisations would have been used the mean value might have been more stable and the effect might only have been noticeable for the lowest time per projections.

5.2 Recovery as a function of disintegration concentration value

Figure 10-15 shows that the recovery does not reach as high values for shorter time per projections, however it can be seen that the recovery stabilizes around DC-value= 11.25 MBq·s/ml which indicates that longer time per projection does not improve the recovery. The graphs shows the importance of measuring recovery coefficients under the same conditions as the image protocol used for patients. If recovery coefficients are

determined with an image protocol with longer time per projection, compared to the clinical protocol, the recovery coefficients can be underestimated.

5.3 Coefficient of variation as a function of disintegration concentration value

Standard deviation divided by the measured disintegration concentration and the true disintegration concentration in the spheres respectively, as a function of DC-value both show that for longer time per projection CV becomes lower, figure 16-21. This is a result of a more stable mean value as the time per projections increases, due to a higher SNR. For all the graphs CV stabilize around DC-value=11.25 MBq·s/ml, but for shorter time per projection CV are relatively large and there are no stable pattern in the data. If discarding tumour 5 there are not a large difference between CV of DC-value=11.25 MBq·s/ml to DC-value=45.00 MBq·s/ml. Again indicating that prolonging the time per projection past DC-value=11.25 MBq·s/ml does not improve the certainty in the mean value in the VOI.

Comparing the two graphs, presented next to each other in figure 16-21, the same pattern is seen for CV compared to the standard deviation divided by the true disintegration concentration. However as the standard deviation is divided with the true disintegration concentration the resulting variance is lower indicating that the largest uncertainty are not due to noise but due to underestimation of the disintegration concentration, i.e. the spillover effect. Thus there are an increasing bias in the recovery as the time per projection is decreased.

Compared to the study by He and Frey [6], on the effects on the accuracy and precision of the quantitative estimates of organ activity as the acquisition time is shortened, the same trend can be seen. With shorter acquisition time an increasing bias is seen and it's more prominent for smaller volumes. The result in this work can also be recognised in the result obtained by Slambrouck et al. on bias reduction for low statistics PET [23]. Even though the PET requires a positron-emitting isotope the image modality is, just as SPECT, a computed tomography system. Thus its reasonably to believe that both systems can display similar effects. Slambrouck et al. [23] showed that for low count statistics, mean value in a region of interest with high activity concentration was underestimated compared to the true mean value when using ML-EM reconstruction. Both of these studies strengthen the result on an increasing bias for lower disintegration concentration i.e. shorter time per projection and the increasing bias as the volumes becomes smaller.

5.4 Accaptance critera

In figures 16-21, Coefficient of variation as a function of disintegration concentration value, the conditions applied to the data are displayed by two solid lines, the black being the highest accepted CV for the tumours and the red being the highest accepted for the kidney. As the standard deviation is divided by the true concentration a larger portion of the data points fulfils the demands, compared to CV. However CV is a more relevant measure of the relative uncertainty because the values form reconstructed images will always be underestimated, due to the spillover effect. The underestimation is typically corrected for with the multiplication of recovery coefficients, but since CV will be unchanged with the multiplication of constants the CV presented in this study give a representative overview of the uncertainty in a corrected concentration as well. Based on the acceptance criterion set to the CV and recovery the data fulfils the DC-values presented in table 4. If excluding contrast C_{sphere}:C_{bkg}=1:0, which is not of clinical relevance because the background uptake in a patient are normally not zero, the DC-value that sets the limit to the lowest possible time per projection is DC-value=22.50 MBq·s/ml for contrast C_{sphere}:C_{bkg}=10:1. Out of the aspect of tumour dosimetry the time per projection can be shortened by a factor 2, but for kidneys the results show the need of increasing the time per projection to 225 seconds, a factor 5 longer than today's protocol. An acquisition time this long is not feasible, so some other solution has to be found. For example could the poor reconstructed noise realisations be evaluated to see if there are connection between where the high max values occur in the image. When looking at one of these reconstructions, high max values were found outside the phantom. If this would be a mutual factor for all the poor reconstructed images a test can be applied to the reconstructed image where its ensured that all activity are inside the phantom, or in the clinical case inside the patient. Otherwise the reconstruction has to be redone. There is also a possibility of setting a limit of how large

fractions can get in the reconstruction algorithm, but since the algorithms in clinical practice normally are provided by the manufacture of the SPECT system this is usually not an option. Another viable option is to change the number of subsets used in the reconstruction. For the current evaluation, the number of subsets was set to 6 with 10 angles per subset. Increasing the number of angles per subset would possibly result in less sensitivity to noisy projection data.

In general the data with lower background levels seemed to be more affected by the shorting in time per projection. This is also believed to be a result of the reconstruction algorithm as the measured projections are divided with the estimated projections. Resulting in poor reconstructed images more frequently.

6 Conclusion

By adding together information from the 113 keV photopeak and the 208 keV photopeak the reduction in acquisition time shows promising results out of the aspect of tumour dosimetry, where the time per projection could be shortened by a factor 2. Contrary to the desired result, dosimery of the kidneys which is the main objective with the image acquisition, did not show a possibility of a shorter acquisition time. The image acquisition 96 hours p.i. need much longer time per projection than used for today's image protocol. The time per projection should be prolonged by a factor 5 to ensure statistical certainty. Since this results in an unreasonable long image acquisition, further work has to be done to strengthen the result in this study and secondarily find an other solution to be able to shorten the acquisition time for today's image protocol and still maintain statistical certainty in the image.

7 Future Work

As mentioned in the discussion (section 5.4) it would be of interest to evaluate the poor reconstructed images to see if there are common factor between them. An other aspect is to modify the reconstruction algorithm by increasing the number of projections per subset, the reconstruction could become more stabile. Hudson and Larkin writes that for projections with high level of statistical noise it is preferred to use less amount of subsets [8].

Seen in the result, the interesting part are mainly in the interval DC-value=45.00-2.81 MBq·s/ml. Thus for further development of the study it would be advisable to study this interval closer.

Out of the clinical aspect it would be of great interest to study projections including both 113+208 keV photons. To reconstruct these projections scattering kernels including both photons would have to be created.

References

[1] *Monte Carlo Calculations in Nuclear Medicine: APPLICATIONS IN DIAGNOSTIC IMAGING (Series in Medical Physics and Biomedical Engineering)*. Taylor & Francis, 1998.

[2] *Quantitative Nuclear Medicine Imaging: Concepts, Requirements and Methods: IAEA Human Health Reports No.9*. INTL ATOMIC ENERGY AGENCY, 2014.

[3] M.E. Daube-Witherspoon. *Nuclear Medicine Physics: A Handbook for Teachers and Students*. INTL ATOMIC ENERGY AGENCY, 2015. Chapter 8.

[4] Science Medicines Health European Medicines Agency. Lutathera. `https://www.ema.europa.eu/en/medicines/human/EPAR/lutathera`, April 2019. Cited: 070719.

[5] Johan Gustafsson, Gustav Brolin, Maurice Cox, Michael Ljungberg, Lena Johansson, and Katarina Sjögreen Gleisner. Uncertainty propagation for SPECT/CT-based renal dosimetry in177lu peptide receptor radionuclide therapy. *Physics in Medicine and Biology*, 60(21):8329–8346, oct 2015.

[6] Bin He and Eric C. Frey. Effects of shortened acquisition time on accuracy and precision of quantitative estimates of organ activitya). *Medical Physics*, 37(4):1807–1815, mar 2010.

[7] Maria Holstensson, Cecilia Hindorf, Michael Ljungberg, Mike Partridge, and Glenn D. Flux. Optimization of energy-window settings for scatter correction in quantitative 111in imaging: Comparison of measurements and monte carlo simulations. *Cancer Biotherapy and Radiopharmaceuticals*, 22(1):136–142, feb 2007.

[8] H.M. Hudson and R.S. Larkin. Accelerated image reconstruction using ordered subsets of projection data. *IEEE Transactions on Medical Imaging*, 13(4):601–609, 1994.

[9] Heribert Hänscheid, Constantin Lapa, Andreas K. Buck, Michael Lassmann, and Rudolf A. Werner. Dose mapping after endoradiotherapy with177lu-DOTATATE/DOTATOC by a single measurement after 4 days. *Journal of Nuclear Medicine*, 59(1):75–81, jun 2017.

[10] G. El Fakhri J. Ouyang. *Nuclear Medicine Physics: A Handbook for Teachers and Students*. INTL ATOMIC ENERGY AGENCY, 2015. Chapter 17.

[11] Magdy M. Khalil. Elements of gamma camera and SPECT systems. In *Basic Sciences of Nuclear Medicine*, pages 155–178. Springer Berlin Heidelberg, 2010.

[12] Magdy M. Khalil. Emission tomography and image reconstruction. In *Basic Sciences of Nuclear Medicine*, pages 259–284. Springer Berlin Heidelberg, 2010.

[13] Glenn F. Knoll. *Radiation Detection and Measurement*. John Wiley & Sons, 2010.

[14] Filip G. Kondev. Table de radionucléides 177lu. `http://www.nucleide.org/DDEP_WG/Nuclides/Lu-177_tables.pdf`, 2003. Cited: 060719.

[15] Kenneth S. Krane. *Introductory Nuclear Physics*. PAPERBACKSHOP UK IMPORT, 1987.

[16] M. Ljungberg, A. Celler, M. W. Konijnenberg, K. F. Eckerman, Y. K. Dewaraja, and K. Sjogreen-Gleisner. MIRD pamphlet no. 26: Joint EANM/MIRD guidelines for quantitative 177lu SPECT applied for dosimetry of radiopharmaceutical therapy. *Journal of Nuclear Medicine*, 57(1):151–162, oct 2015.

[17] Michael Ljungberg. Quantitative SPECT imaging. In *Basic Sciences of Nuclear Medicine*, pages 285–309. Springer Berlin Heidelberg, 2010.

[18] Michael Ljungberg, Katarina Sjögreen, Xiaowei Liu, Eric Frey, Yuni Dewaraja, and Sven-Erik Strand. A 3-dimensional absorbed dose calculation method based on quantitative spect for radionuclide therapy: evaluation for (131)i using monte carlo simulation. *Journal of nuclear medicine : official publication, Society of Nuclear Medicine*, 43:1101–1109, August 2002.

[19] M.G. Lötter. *Nuclear Medicine Physics: A Handbook for Teachers and Students*. INTL ATOMIC ENERGY AGENCY, 2015. Chapter 5.

[20] R. Stephenson R.J. Ott. *Nuclear Medicine Physics: A Handbook for Teachers and Students*. INTL ATOMIC ENERGY AGENCY, 2015. Chapter 7.

[21] Tobias L. Roß and Simon M. Ametamey. PET chemistry: Radiopharmaceuticals. In *Basic Sciences of Nuclear Medicine*, pages 103–118. Springer Berlin Heidelberg, 2010.

[22] Tamer B. Saleh. Radiopharmacy: Basics. In *Basic Sciences of Nuclear Medicine*, pages 25–39. Springer Berlin Heidelberg, 2010.

[23] Katrien Van Slambrouck, Simon Stute, Claude Comtat, Merence Sibomana, Floris H. P. van Velden, Ronald Boellaard, and Johan Nuyts. Bias reduction for low-statistics PET: Maximum likelihood reconstruction with a modified poisson distribution. *IEEE Transactions on Medical Imaging*, 34(1):126–136, jan 2015.

[24] National Data Center website. Nudat2.6. `https://www.nndc.bnl.gov/nudat2/decaysearchdirect.jsp?nuc=177LU&unc=nds`. Cited: 070719.

A Additional Result

A.1 Recovery as a function of sphere volume

Figure 22-25 present the recovery as a function of sphere volume for 208 keV with the four different contrasts C_{sphere}:C_{bkg} and including all 10 DC-values. The error bars display the error of the mean of the 50 noise realisations divided with the true disintegration concentration. Photon energy 113 keV are presented in figure 26-29 and 113+208 keV are presented in figure 30-33. The recovery is calculated by the mean disintegration concentration in the VOI.

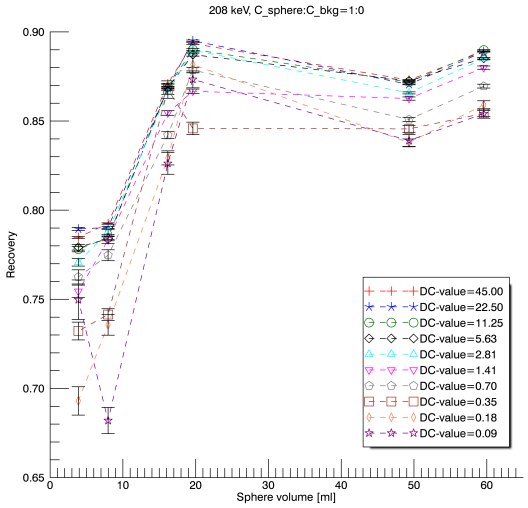

Figure 22: *Recovery as a function of volume of the spheres for 208 keV photons and contrast C_{sphere}:C_{bkg}=1:0.*

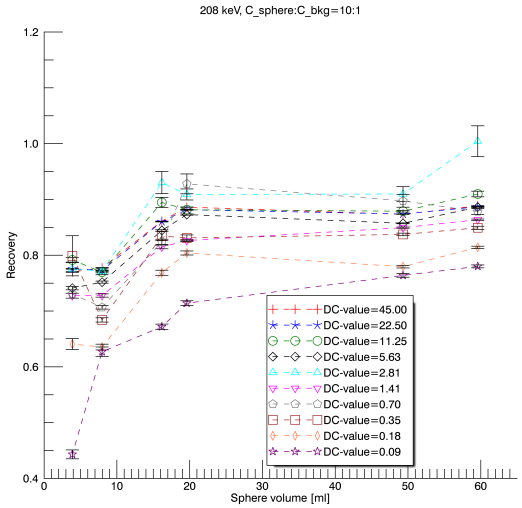

Figure 23: *Recovery as a function of volume of the spheres for 208 keV photons and contrast C_{sphere}:C_{bkg}=10:1.*

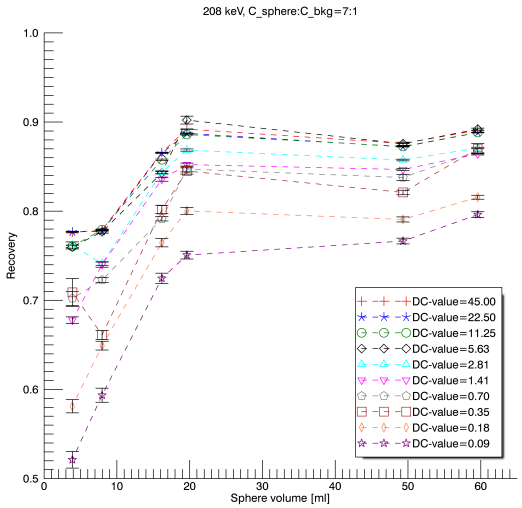

Figure 24: *Recovery as a function of volume of the spheres for 208 keV photons and contrast* C_{sphere}*:*C_{bkg}*=7:1.*

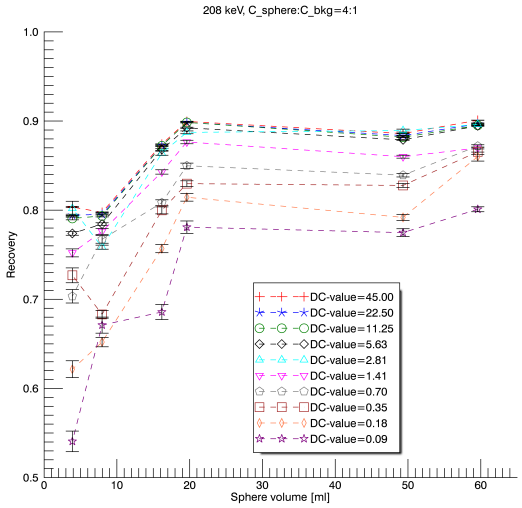

Figure 25: *Recovery as a function of volume of the spheres for 208 keV photons and contrast* C_{sphere}*:*C_{bkg}*=4:1.*

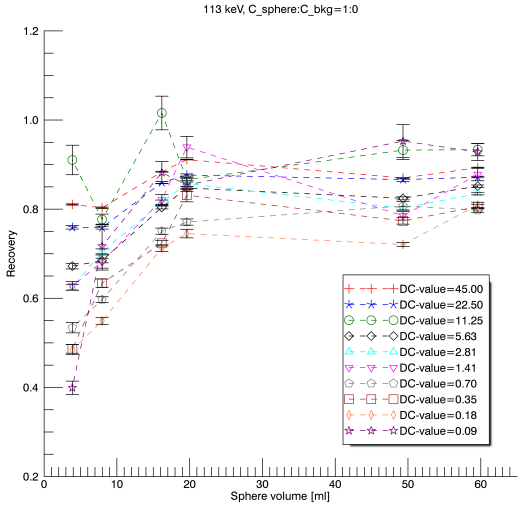

Figure 26: *Recovery as a function of volume of the spheres for 113 keV photons and contrast* C_{sphere}:C_{bkg}*=1:0.*

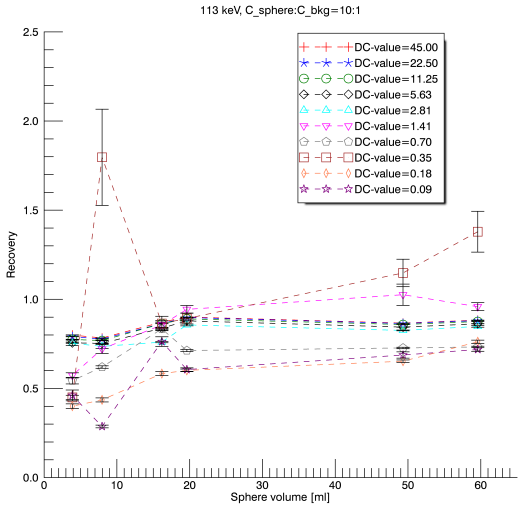

Figure 27: *Recovery as a function of volume of the spheres for 113 keV photons and contrast* C_{sphere}:C_{bkg}*=10:1.*

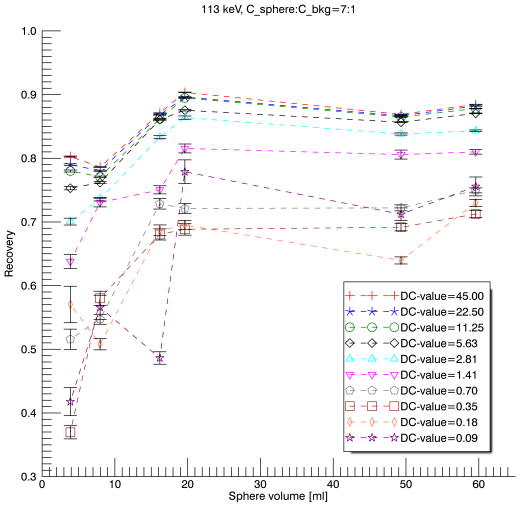

Figure 28: *Recovery as a function of volume of the spheres for 113 keV photons and contrast* C_{sphere}*:*C_{bkg}*=7:1.*

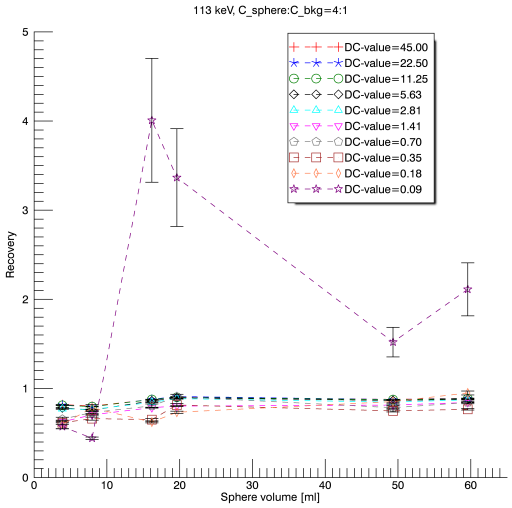

Figure 29: *Recovery as a function of volume of the spheres for 113 keV photons and contrast* C_{sphere}*:*C_{bkg}*=4:1.*

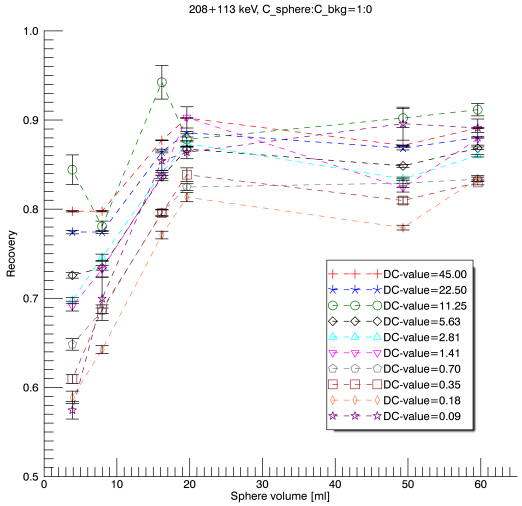

Figure 30: *Recovery as a function of volume of the spheres for 113 and 208 keV photons and contrast* C_{sphere}*:*C_{bkg}*=1:0.*

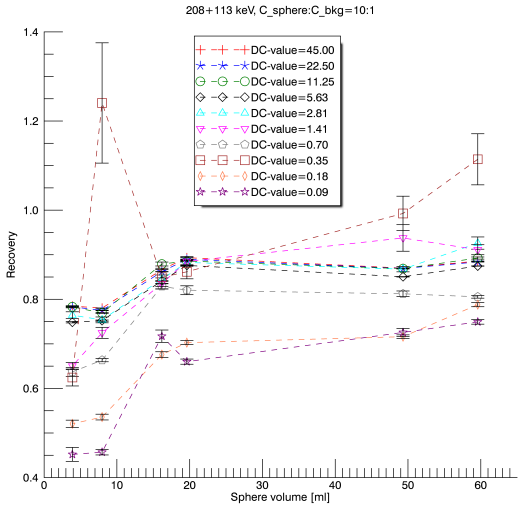

Figure 31: *Recovery as a function of volume of the spheres for 113 and 208 keV photons and contrast* C_{sphere}*:*C_{bkg}*=10:1.*

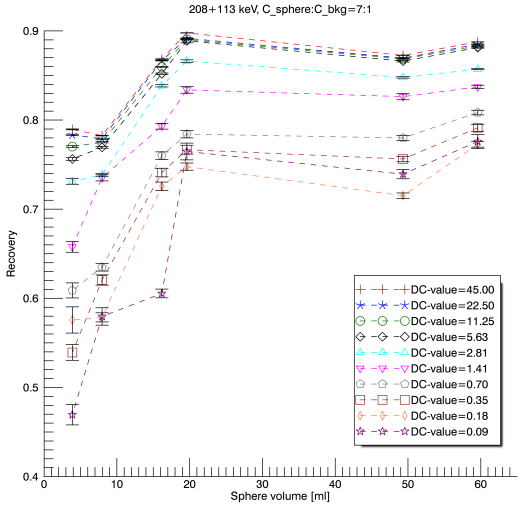

Figure 32: *Recovery as a function of volume of the spheres for 113 and 208 keV photons and contrast C_{sphere}:C_{bkg}=7:1.*

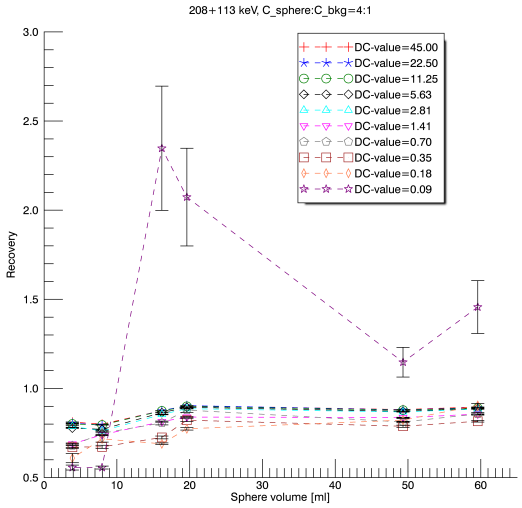

Figure 33: *Recovery as a function of volume of the spheres for 113 and 208 keV photons and contrast C_{sphere}:C_{bkg}=4:1.*

A.2 Recovery as a function of disintegration concentration constant

The recovery calculated by the mean disintegration concentration in a VOI is presented as a function of DC-value for all four contrast ratio C_{sphere}:C_{bkg}. Figure 34-37 displays the result for 208 keV, figure 38-41 displays 113 keV and 42-45 displays 113+208 keV. The error bars display the error of the mean of the 50 noise realisations divided with the true disintegration concentration.

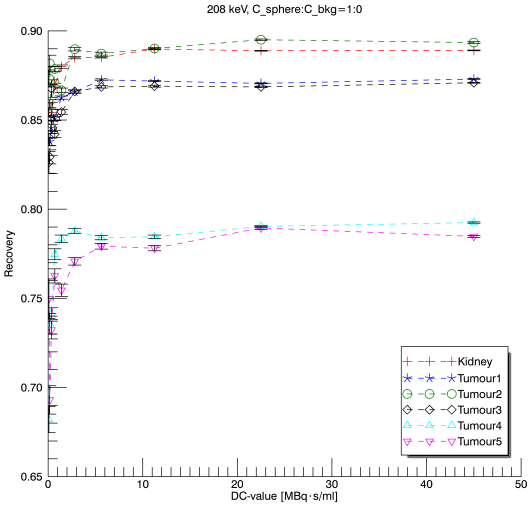

Figure 34: *Recovery as a function of DC-value for 208 keV photons and contrast C_{sphere}:C_{bkg}=1:0.*

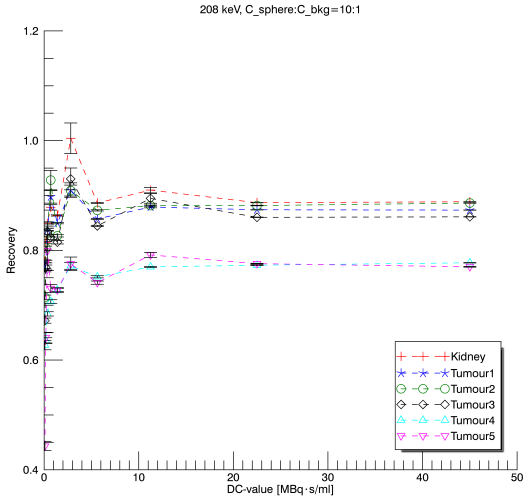

Figure 35: *Recovery as a function of DC-value for 208 keV photons and contrast C_{sphere}:C_{bkg}=10:1.*

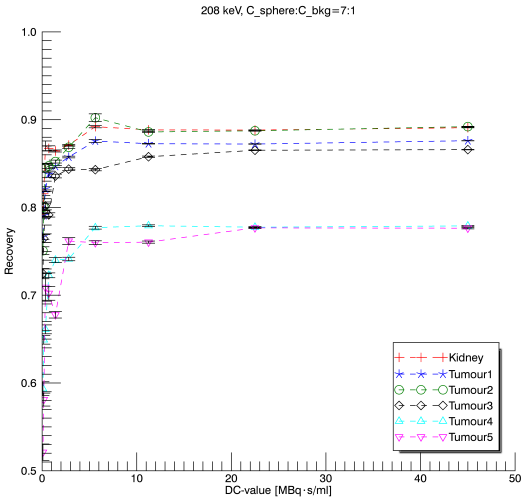

Figure 36: *Recovery as a function of DC-value for 208 keV photons and contrast C_{sphere}:C_{bkg}=7:1.*

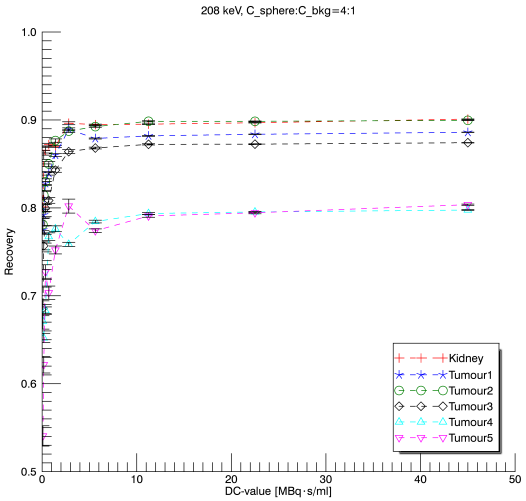

Figure 37: *Recovery as a function of DC-value for 208 keV photons and contrast C_{sphere}:C_{bkg}=4:1.*

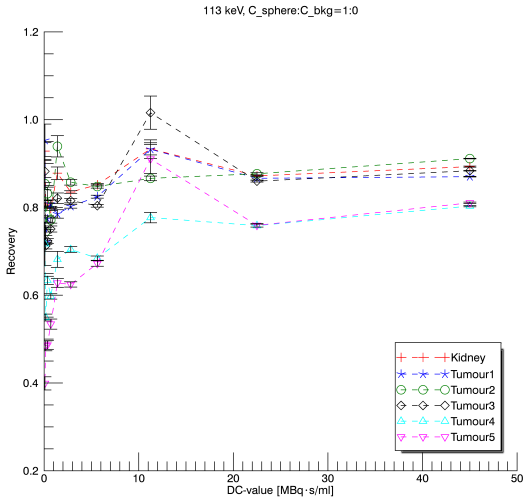

Figure 38: *Recovery as a function of DC-value for 113 keV photons and contrast C_{sphere}:C_{bkg}=1:0.*

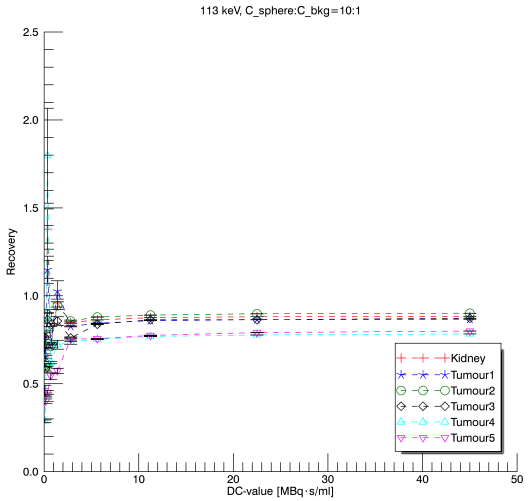

Figure 39: *Recovery as a function of DC-value for 113 keV photons and contrast C_{sphere}:C_{bkg}=10:1.*

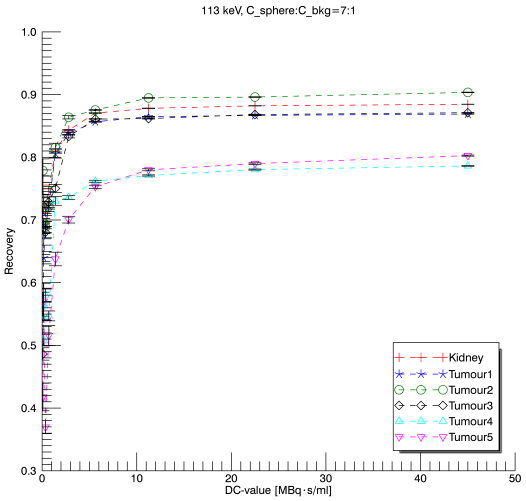

Figure 40: *Recovery as a function of DC-value for 113 keV photons and contrast C_{sphere}:C_{bkg}=7:1.*

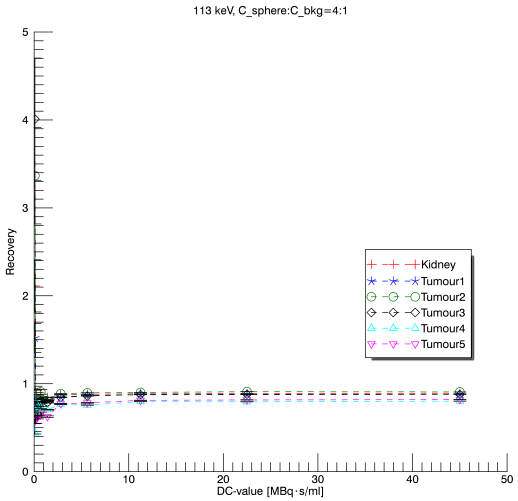

Figure 41: *Recovery as a function of DC-value for 113 keV photons and contrast C_{sphere}:C_{bkg}=4:1.*

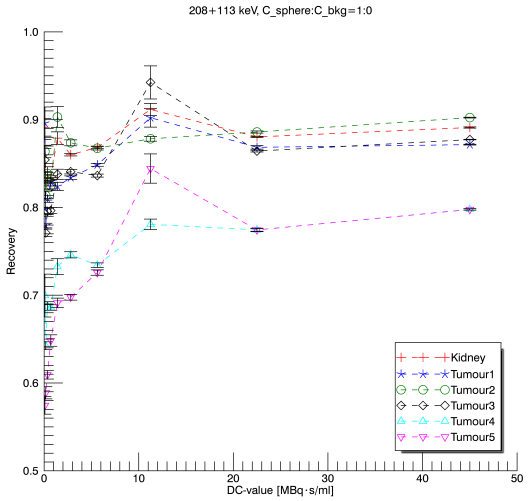

Figure 42: *Recovery as a function of DC-value for 113 and 208 keV photons and contrast C_{sphere}:C_{bkg}=1:0.*

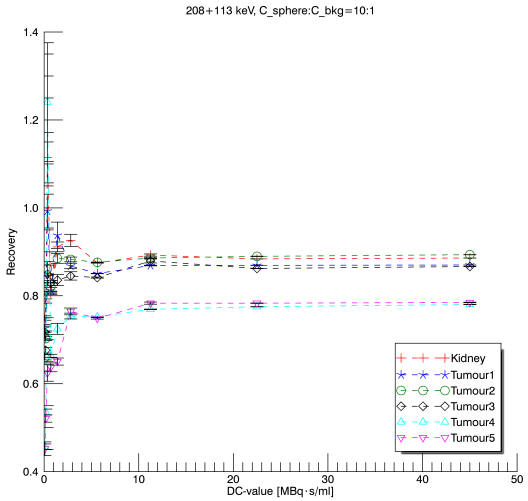

Figure 43: *Recovery as a function of DC-value for 113 and 208 keV photons and contrast C_{sphere}:C_{bkg}=10:1.*

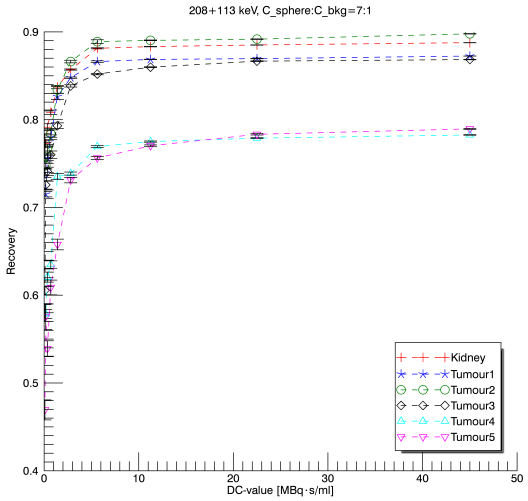

Figure 44: *Recovery as a function of DC-value for 113 and 208 keV photons and contrast C_{sphere}:C_{bkg}=7:1.*

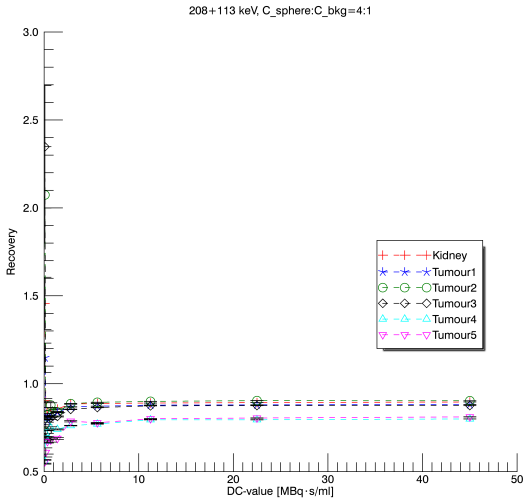

Figure 45: *Recovery as a function of DC-value for 113 and 208 keV photons and contrast C_{sphere}:C_{bkg}=4:1.*

A.3 Coefficient of variation as a function of disintegration concentration value

The following figures display CV, in decimal form, as a function of DC-value. For comparison the standard deviation is both divided with the measured disintegration concentration and true disintegration concentration, respectively. The two graphs, for one photon energy and contrast C_{sphere}:C_{bkg}, are presented next to each other. Figures 46-47 presents result for 208 keV, figures 50-53, 53 presents results for 113 keV and figures 54-57 presents result for 113+208 keV.

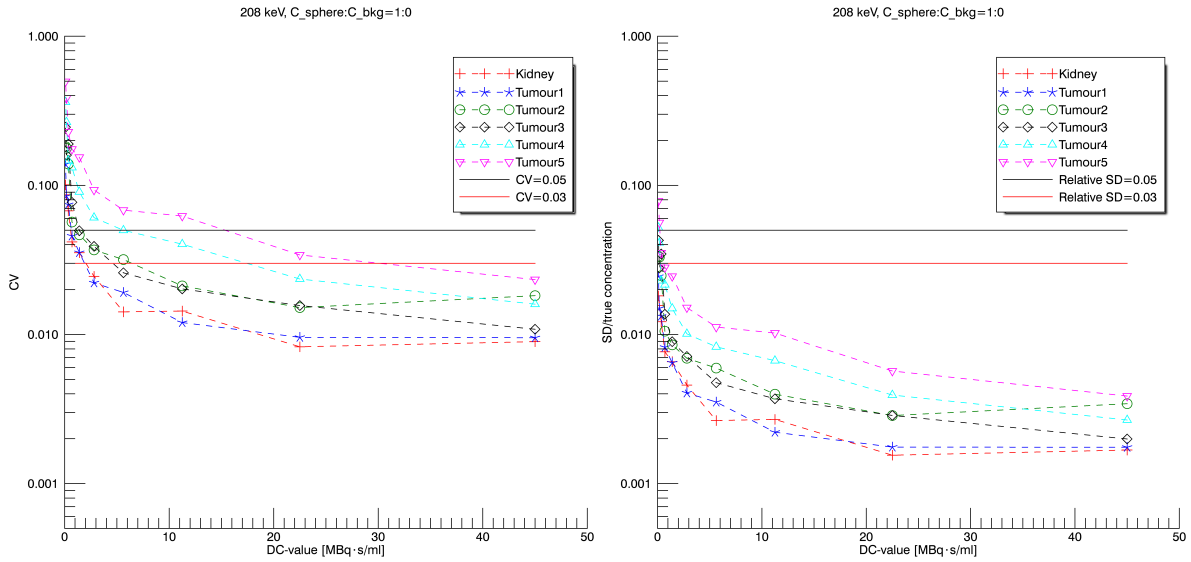

Figure 46: *For 208 keV photons and contrast C_{sphere}:C_{bkg}=1:0. Left graph present CV, standard deviation divided by the measured disintegration concentration in the spheres, as a function of DC-value. Right graph present the standard deviation divided by the true disintegration concentration in the spheres, as a function of DC-value.*

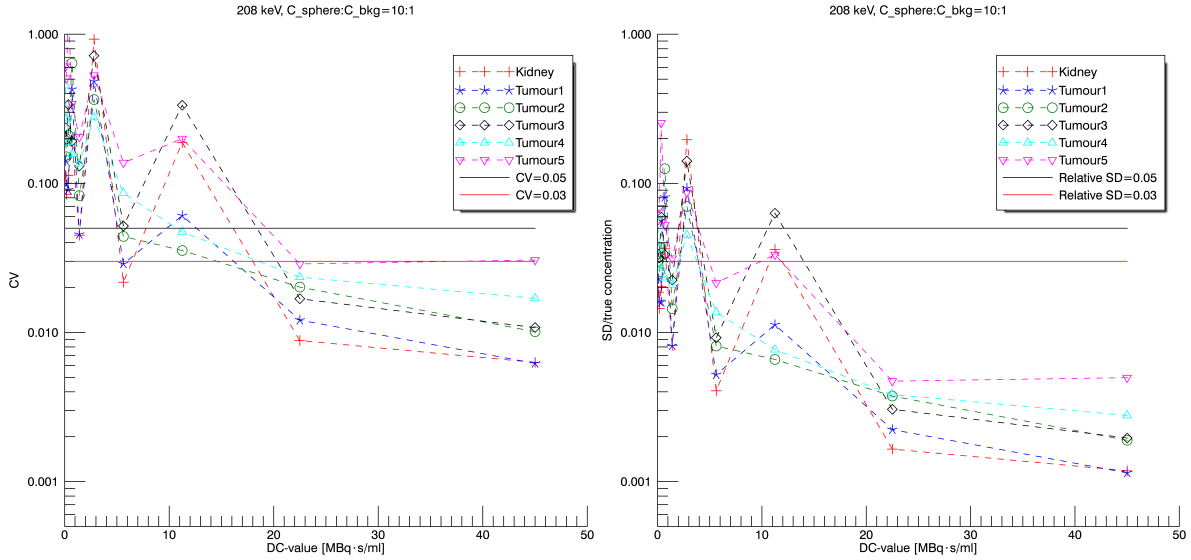

Figure 47: *For 208 keV photons and contrast C_{sphere}:C_{bkg}=10:1. Left graph present CV, standard deviation divided by the measured disintegration concentration in the spheres, as a function of DC-value. Right graph present the standard deviation divided by the true disintegration concentration in the spheres, as a function of DC-value.*

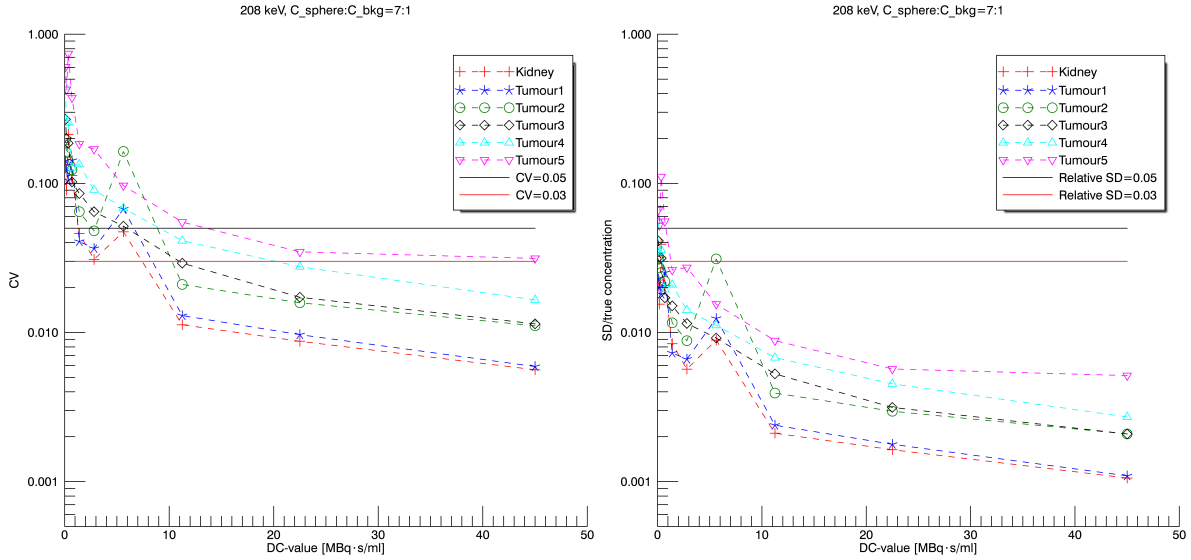

Figure 48: *For 208 keV photons and contrast C_{sphere}:C_{bkg}=7:1. Left graph present CV, standard deviation divided by the measured disintegration concentration in the spheres, as a function of DC-value. Right graph present the standard deviation divided by the true disintegration concentration in the spheres, as a function of DC-value.*

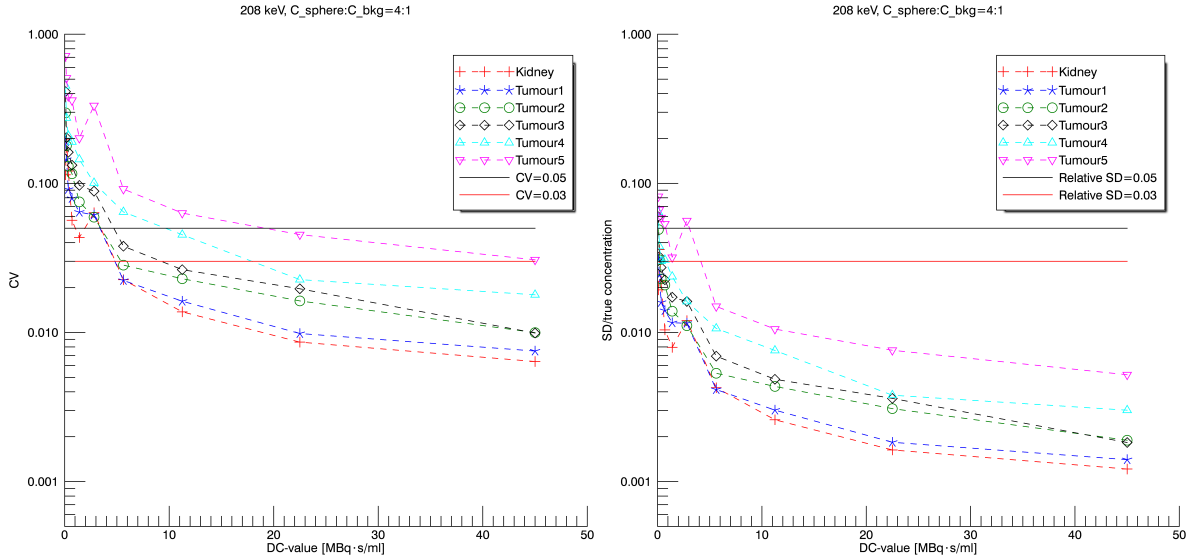

Figure 49: *For 208 keV photons and contrast C_{sphere}:C_{bkg}=4:1. Left graph present CV, standard deviation divided by the measured disintegration concentration in the spheres, as a function of DC-value. Right graph present the standard deviation divided by the true disintegration concentration in the spheres, as a function of DC-value.*

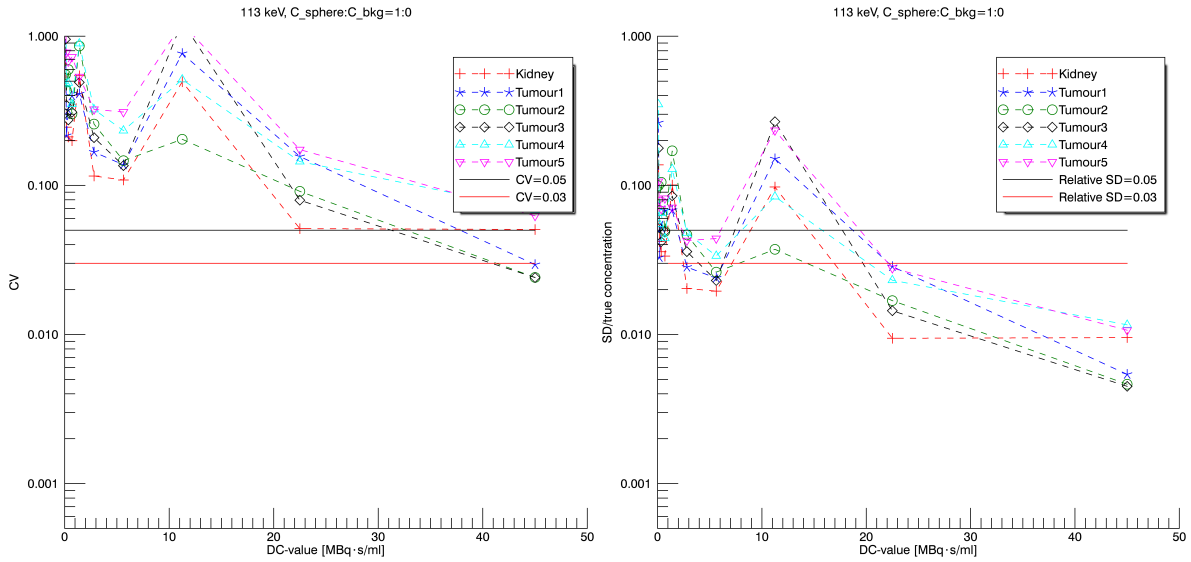

Figure 50: *For 113 keV photons and contrast C_{sphere}:C_{bkg}=1:0. Left graph present CV, standard deviation divided by the measured disintegration concentration in the spheres, as a function of DC-value. Right graph present the standard deviation divided by the true disintegration concentration in the spheres, as a function of DC-value.*

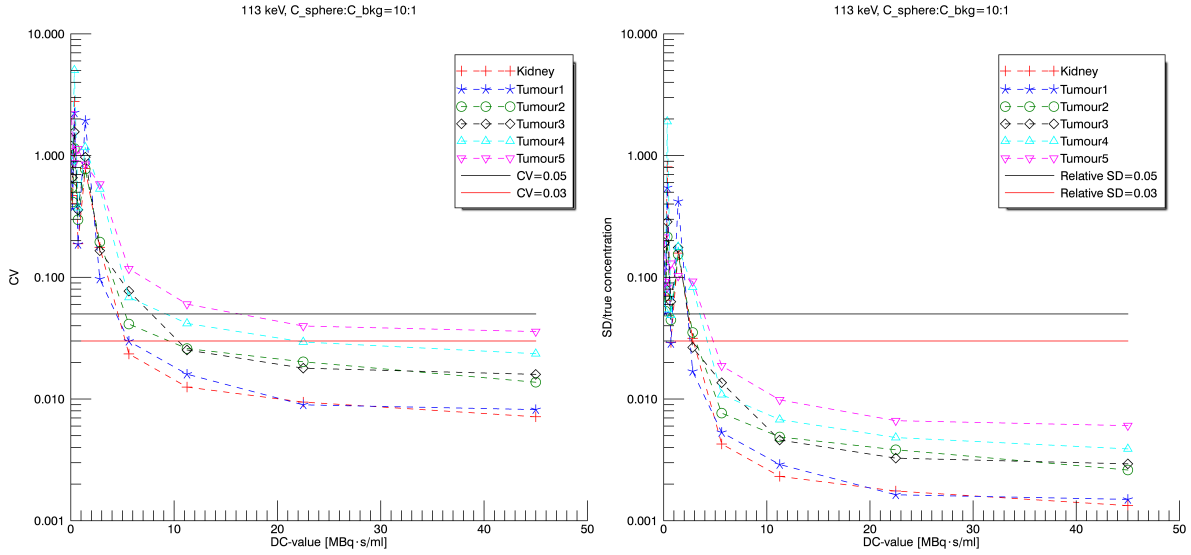

Figure 51: *For 113 keV photons and contrast C_{sphere}:C_{bkg}=10:1. Left graph present CV, standard deviation divided by the measured disintegration concentration in the spheres, as a function of DC-value. Right graph present the standard deviation divided by the true disintegration concentration in the spheres, as a function of DC-value.*

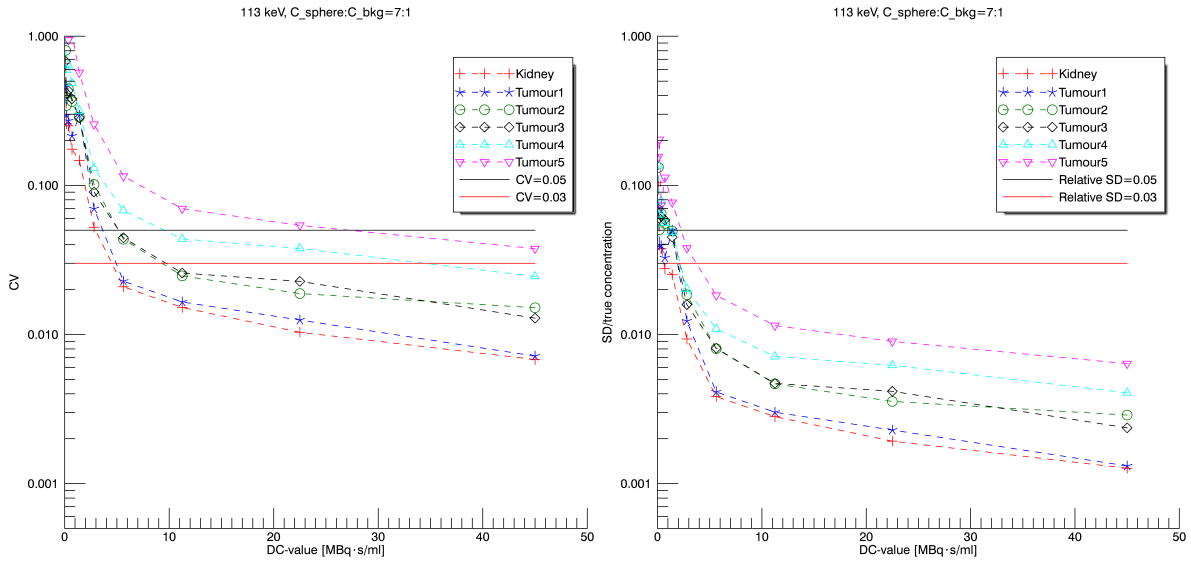

Figure 52: *For 113 keV photons and contrast C_{sphere}:C_{bkg}=7:1. Left graph present CV, standard deviation divided by the measured disintegration concentration in the spheres, as a function of DC-value. Right graph present the standard deviation divided by the true disintegration concentration in the spheres, as a function of DC-value.*

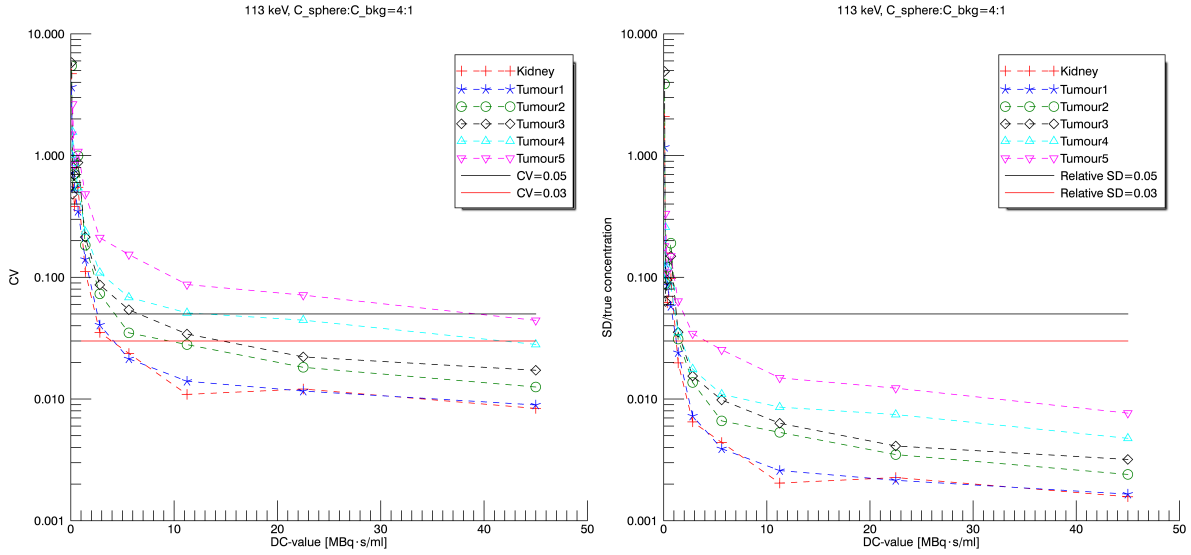

Figure 53: *For 113 keV photons and contrast C_{sphere}:C_{bkg}=4:1. Left graph present CV, standard deviation divided by the measured disintegration concentration in the spheres, as a function of DC-value. Right graph present the standard deviation divided by the true disintegration concentration in the spheres, as a function of DC-value.*

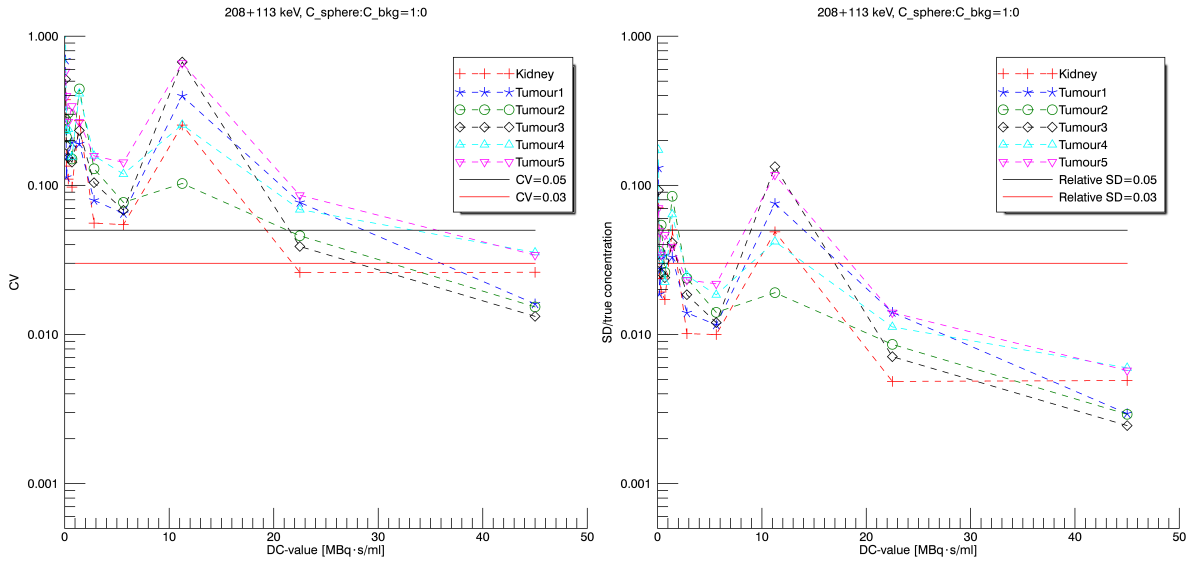

Figure 54: *For 113 and 208 keV photons and contrast C_{sphere}:C_{bkg}=1:0. Left graph present CV, standard deviation divided by the measured disintegration concentration in the spheres, as a function of DC-value. Right graph present the standard deviation divided by the true disintegration concentration in the spheres, as a function of DC-value.*

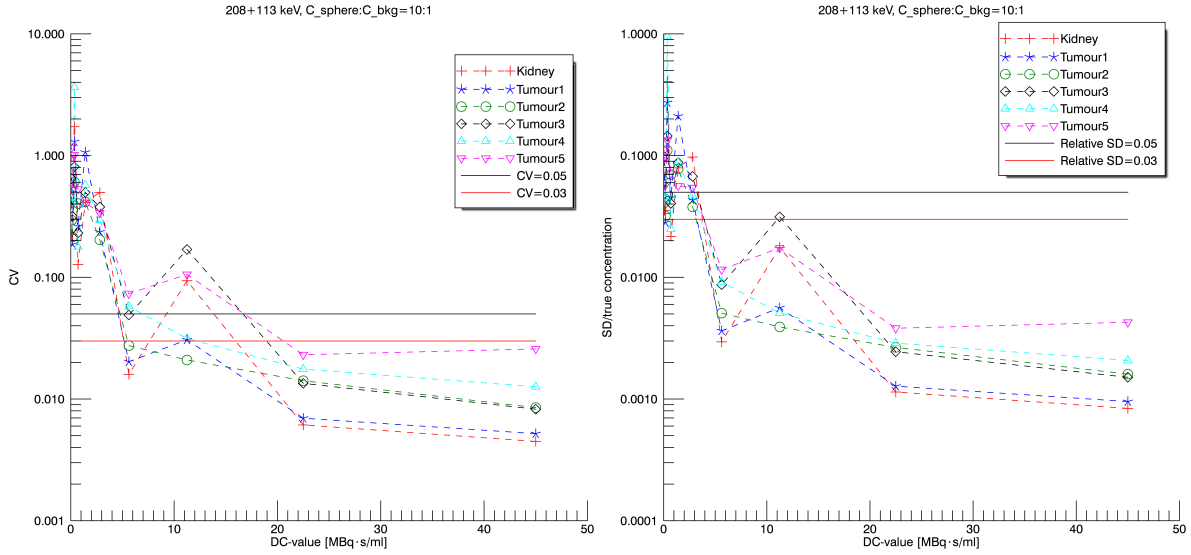

Figure 55: *For 113 and 208 keV photons and contrast C_{sphere}:C_{bkg}=10:1. Left graph present CV, standard deviation divided by the measured disintegration concentration in the spheres, as a function of DC-value. Right graph present the standard deviation divided by the true disintegration concentration in the spheres, as a function of DC-value.*

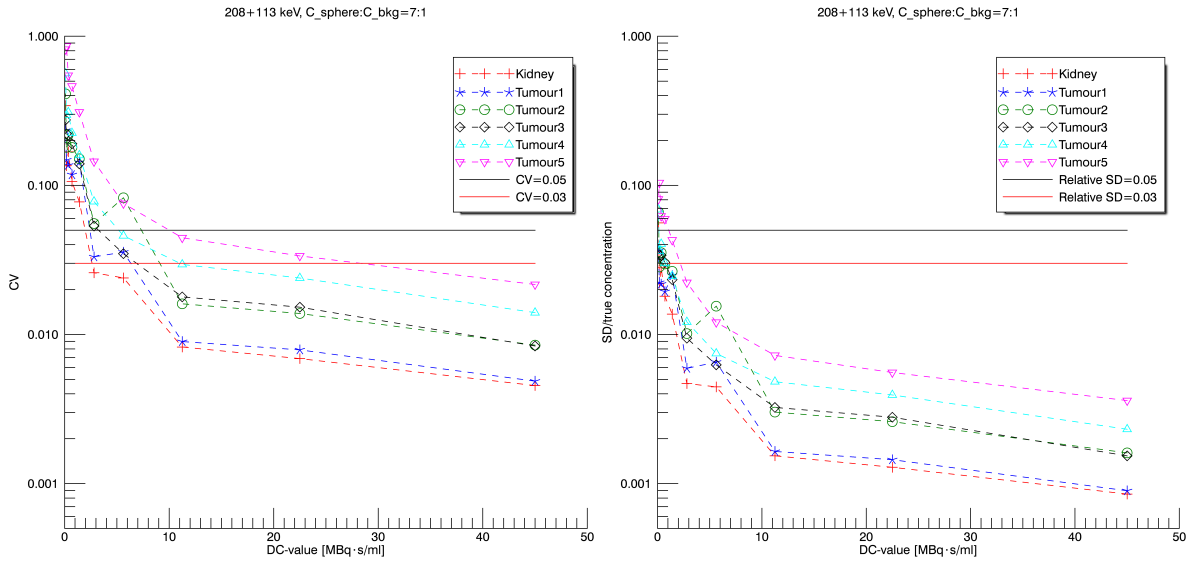

Figure 56: *For 113 and 208 keV photons and contrast C_{sphere}:C_{bkg}=7:1. Left graph present CV, standard deviation divided by the measured disintegration concentration in the spheres, as a function of DC-value. Right graph present the standard deviation divided by the true disintegration concentration in the spheres, as a function of DC-value.*

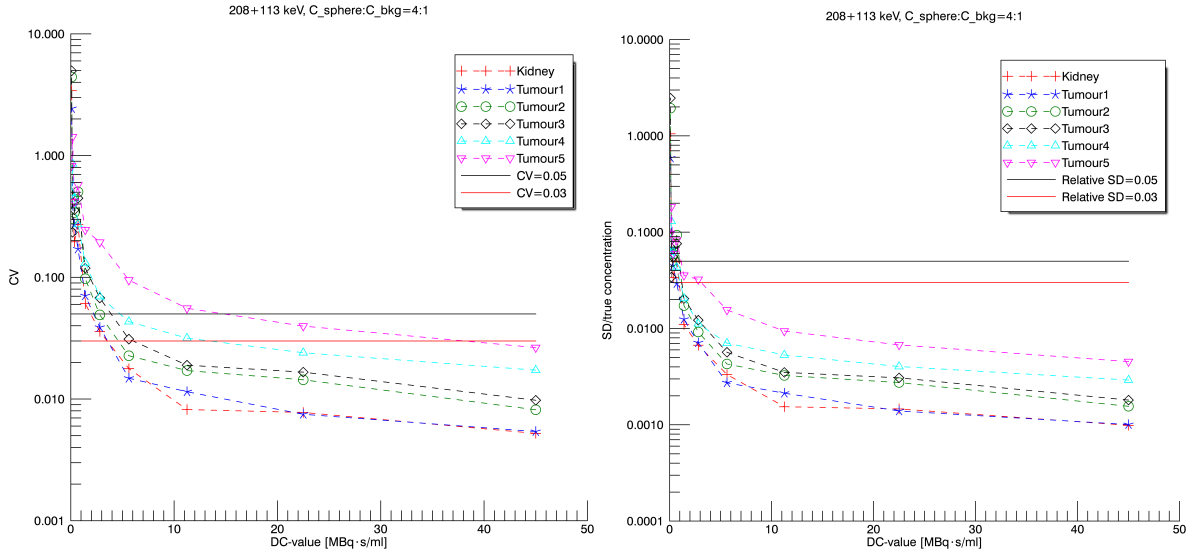

Figure 57: *For 113 and 208 keV photons and contrast C_{sphere}:C_{bkg}=4:1. Left graph present CV, standard deviation divided by the measured disintegration concentration in the spheres, as a function of DC-value. Right graph present the standard deviation divided by the true disintegration concentration in the spheres, as a function of DC-value.*

A.4 Acceptance Criteria

Acceptance criteria fulfilment, according to acceptance criterion in table 3, for every photon energy and contrast C_{sphere}:C_{bkg} are presented in table 5-16. The data demands are fulfilled for value 1 and not fulfilled for value 0.

Table 5: *Acceptance criteria fulfilment for 208 keV, C_{sphere}:C_{bkg}=1:4.*

DC-value	45.00	22.50	11.25	5.63	2.81	1.41	0.70	0.35	0.18	0.09
Kidney	1	1	1	1	0	0	0	0	0	0
Tumour 1	1	1	1	1	0	0	0	0	0	0
Tumour 2	1	1	1	1	0	0	0	0	0	0
Tumour 3	1	1	1	1	0	0	0	0	0	0
Tumour 4	1	1	1	0	0	0	0	0	0	0
Tumour 5	1	1	0	0	0	0	0	0	0	0

Table 6: *Acceptance criteria fulfilment for 208 keV, C_{sphere}:C_{bkg}=1:7.*

DC-value	45.00	22.50	11.25	5.63	2.81	1.41	0.70	0.35	0.18	0.09
Kidney	1	1	1	0	0	0	0	0	0	0
Tumour 1	1	1	1	0	1	1	0	0	0	0
Tumour 2	1	1	1	0	1	0	0	0	0	0
Tumour 3	1	1	1	0	0	0	0	0	0	0
Tumour 4	1	1	1	0	0	0	0	0	0	0
Tumour 5	1	1	0	0	0	0	0	0	0	0

Table 7: *Acceptance criteria fulfilment for 208 keV, C_{sphere}:C_{bkg}=1:10.*

DC-value	45.00	22.50	11.25	5.63	2.81	1.41	0.70	0.35	0.18	0.09
Kidney	1	1	0	1	0	0	0	0	0	0
Tumour 1	1	1	0	1	0	1	0	0	0	0
Tumour 2	1	1	1	1	0	0	0	0	0	0
Tumour 3	1	1	0	0	0	0	0	0	0	0
Tumour 4	1	1	1	0	0	0	0	0	0	0
Tumour 5	1	1	0	0	0	0	0	0	0	0

Table 8: *Acceptance criteria fulfilment for 208 keV, C_{sphere}:C_{bkg}=1:0.*

DC-value	45.00	22.50	11.25	5.63	2.81	1.41	0.70	0.35	0.18	0.09
Kidney	1	1	1	1	1	0	0	0	0	0
Tumour 1	1	1	1	1	1	1	1	0	0	0
Tumour 2	1	1	1	1	1	1	0	0	0	0
Tumour 3	1	1	1	1	1	1	0	0	0	0
Tumour 4	1	1	1	1	0	0	0	0	0	0
Tumour 5	1	1	0	0	0	0	0	0	0	0

Table 9: *Acceptance criteria fulfilment for 113 keV, C_{sphere}:C_{bkg}=1:4.*

DC-value	45.00	22.50	11.25	5.63	2.81	1.41	0.70	0.35	0.18	0.09
Kidney	1	1	1	1	0	0	0	0	0	0
Tumour 1	1	1	1	1	1	0	0	0	0	0
Tumour 2	1	1	1	1	0	0	0	0	0	0
Tumour 3	1	1	1	0	0	0	0	0	0	0
Tumour 4	1	1	0	0	0	0	0	0	0	0
Tumour 5	1	0	0	0	0	0	0	0	0	0

Table 10: *Acceptance criteria fulfilment for 113 keV, C_{sphere}:C_{bkg}=1:7.*

DC-value	45.00	22.50	11.25	5.63	2.81	1.41	0.70	0.35	0.18	0.09
Kidney	1	1	1	1	0	0	0	0	0	0
Tumour 1	1	1	1	1	0	0	0	0	0	0
Tumour 2	1	1	1	1	0	0	0	0	0	0
Tumour 3	1	1	1	1	0	0	0	0	0	0
Tumour 4	1	1	1	0	0	0	0	0	0	0
Tumour 5	1	0	0	0	0	0	0	0	0	0

Table 11: *Acceptance criteria fulfilment for 113 keV, C_{sphere}:C_{bkg}=1:10.*

DC-value	45.00	22.50	11.25	5.63	2.81	1.41	0.70	0.35	0.18	0.09
Kidney	1	1	1	1	0	0	0	0	0	0
Tumour 1	1	1	1	1	0	0	0	0	0	0
Tumour 2	1	1	1	1	0	0	0	0	0	0
Tumour 3	1	1	1	0	0	0	0	0	0	0
Tumour 4	1	1	1	0	0	0	0	0	0	0
Tumour 5	1	1	0	0	0	0	0	0	0	0

Table 12: *Acceptance criteria fulfilment for 113 keV, C_{sphere}:C_{bkg}=1:0.*

DC-value	45.00	22.50	11.25	5.63	2.81	1.41	0.70	0.35	0.18	0.09
Kidney	0	0	0	0	0	0	0	0	0	0
Tumour 1	1	0	0	0	0	0	0	0	0	0
Tumour 2	1	0	0	0	0	0	0	0	0	0
Tumour 3	1	0	0	0	0	0	0	0	0	0
Tumour 4	0	0	0	0	0	0	0	0	0	0
Tumour 5	0	0	0	0	0	0	0	0	0	0

Table 13: *Acceptance criteria fulfilment for 113+208 keV, C_{sphere}:C_{bkg}=1:4.*

DC-value	45.00	22.50	11.25	5.63	2.81	1.41	0.70	0.35	0.18	0.09
Kidney	1	1	1	1	0	0	0	0	0	0
Tumour 1	1	1	1	1	1	0	0	0	0	0
Tumour 2	1	1	1	1	1	0	0	0	0	0
Tumour 3	1	1	1	1	0	0	0	0	0	0
Tumour 4	1	1	1	1	0	0	0	0	0	0
Tumour 5	1	1	0	0	0	0	0	0	0	0

Table 14: *Acceptance criteria fulfilment for 113+208 keV, C_{sphere}:C_{bkg}=1:7.*

DC-value	45.00	22.50	11.25	5.63	2.81	1.41	0.70	0.35	0.18	0.09
Kidney	1	1	1	1	1	0	0	0	0	0
Tumour 1	1	1	1	1	1	0	0	0	0	0
Tumour 2	1	1	1	0	0	0	0	0	0	0
Tumour 3	1	1	1	1	0	0	0	0	0	0
Tumour 4	1	1	1	1	0	0	0	0	0	0
Tumour 5	1	1	1	0	0	0	0	0	0	0

Table 15: *Acceptance criteria fulfilment for 113+208 keV, C_{sphere}:C_{bkg}=1:10.*

DC-value	45.00	22.50	11.25	5.63	2.81	1.41	0.70	0.35	0.18	0.09
Kidney	1	1	0	1	0	0	0	0	0	0
Tumour 1	1	1	1	1	0	0	0	0	0	0
Tumour 2	1	1	1	1	0	0	0	0	0	0
Tumour 3	1	1	1	1	0	0	0	0	0	0
Tumour 4	1	1	1	0	0	0	0	0	0	0
Tumour 5	1	1	0	0	0	0	0	0	0	0

Table 16: *Acceptance criteria fulfilment for 113+208 keV, C_{sphere}:C_{bkg}=1:0.*

DC-value	45.00	22.50	11.25	5.63	2.81	1.41	0.70	0.35	0.18	0.09
Kidney	1	1	0	0	0	0	0	0	0	0
Tumour 1	1	0	0	0	0	0	0	0	0	0
Tumour 2	1	1	0	0	0	0	0	0	0	0
Tumour 3	1	1	0	0	0	0	0	0	0	0
Tumour 4	1	0	0	0	0	0	0	0	0	0
Tumour 5	1	0	0	0	0	0	0	0	0	0